

1 **Genomic instability caused by Arp2/3 complex inactivation results in**  
2 **micronucleus biogenesis and cellular senescence**

3

4 Running Title: Arp2/3 complex inactivation and senescence

5

6

7 **Elena L. Haarer<sup>1,2</sup>, Shirley Guo<sup>1,2</sup>, and Kenneth G. Campellone<sup>1,2,3,\*</sup>**

8

9

10 <sup>1</sup>Department of Molecular and Cell Biology;

11 <sup>2</sup>Institute for Systems Genomics;

12 <sup>3</sup>Center on Aging, UConn Health;

13 University of Connecticut, Storrs CT, USA

14

15 \*Corresponding Author

16 E-mail: [kenneth.campellone@uconn.edu](mailto:kenneth.campellone@uconn.edu)

## 17 **Abstract**

18 The Arp2/3 complex is a ubiquitous actin nucleator with well-characterized activities in cell  
19 organization and movement, but its roles in chromatin-associated and cell cycle-related  
20 processes are relatively understudied. We investigated how the Arp2/3 complex affects  
21 genomic integrity, mitosis, and cell proliferation using mouse fibroblasts containing an inducible  
22 knockout (iKO) of the ArpC2 subunit. We show that permanent Arp2/3 ablation results in DNA  
23 damage, the formation of cytosolic micronuclei, and cellular senescence. Upon Arp2/3  
24 depletion, cells undergo an abrupt proliferation arrest that is accompanied by activation of the  
25 tumor suppressor p53, upregulation of its downstream cell cycle inhibitor *Cdkn1a/p21*, and  
26 recognition of micronuclei by the cytosolic DNA sensor cGAS. Micronuclei arise in ArpC2 iKO  
27 cells due to chromosome segregation defects during mitosis and premature mitotic exits. Such  
28 phenotypes are explained by the presence of damaged chromatin fragments that fail to attach to  
29 the mitotic spindle, abnormalities in actin assembly during metaphase, and asymmetric  
30 microtubule architecture during anaphase. These studies establish functional requirements for  
31 the mammalian Arp2/3 complex in genome stability and mitotic spindle organization. They  
32 further expand our understanding of the intracellular mechanisms that lead to senescence and  
33 suggest that cytoskeletal dysfunction is an underlying factor in biological aging.

## 34 **Author Summary**

35 The actin cytoskeleton consists of protein polymers that assemble and disassemble to control  
36 the organization, shape, and movement of cells. However, relatively little is understood about  
37 how the actin cytoskeleton affects genome maintenance, cell multiplication, and biological  
38 aging. In this study, we show that knocking out the Arp2/3 complex, a core component of the  
39 actin assembly machinery, causes DNA damage, genomic instability, defects in chromosome  
40 partitioning during mitosis, and a permanent cell proliferation arrest called senescence. Since  
41 senescent cells are major contributors to both age-associated diseases and tumor suppression,  
42 our findings open new avenues of investigation into how natural or experimental alterations of  
43 cytoskeletal proteins impact the process of aging and the regulation of cancer.

## 44 Introduction

45 The actin cytoskeleton consists of dynamic protein polymers that have well-known functions in  
46 cell morphogenesis and motility. Globular (G-) actin monomers are present in the cytoplasm  
47 and nucleus, and their polymerization into filamentous (F-) actin is driven by proteins called  
48 nucleators [1]. These include actin monomer-oligomerizing proteins, Formin-family  
49 nucleation/elongation proteins, and the Arp2/3 complex – a heteroheptameric actin assembly  
50 factor that binds to the sides of existing filaments and nucleates new filaments to create  
51 branched networks [2]. The Arp2/3 complex is highly conserved across almost all eukaryotes  
52 [3,4] and is required for viability in such organisms; inactivation of genes encoding its subunits  
53 prevents growth of *S.cerevisiae* [5,6] and *D.discoideum* [7] and is embryonic lethal in animals  
54 including *D.melanogaster* [8,9], *C.elegans* [10,11], and *M.musculus* [12-14]. However, the  
55 cellular basis underlying the essential nature of the Arp2/3 complex is not well understood.

56 Many processes that involve plasma membrane dynamics, especially cell adhesion and  
57 motility, rely on actin networks assembled by the Arp2/3 complex [15]. In fact, conditional  
58 knockouts in mice indicate that the complex is crucial for maintaining normal tissue architecture,  
59 promoting changes in cell shape, and powering cell migration during development [14,16-20].  
60 These *in vivo* results are consistent with molecular and cellular studies of Arp2/3-mediated actin  
61 assembly using *in vitro* systems [21], dominant negative regulatory proteins [22], transient  
62 RNAi-mediated knockdowns [23], and pharmacological inhibitors of the complex [24,25].

63 In contrast to the well-characterized roles of the Arp2/3 complex in protrusion and  
64 motility, its functions in nuclear processes are only beginning to emerge. During interphase, all  
65 3 classes of actin nucleators promote nuclear actin filament assembly in response to acute DNA  
66 damaging agents [26-28]. In the nuclei of *Drosophila* and mammalian cells, Arp2/3-mediated  
67 actin polymerization is crucial for repositioning damaged heterochromatin to the nuclear  
68 periphery, which enables subsequent DNA repair activities [27,28]. As a result, depletion of the

69 Arp2/3 complex using RNAi in *Drosophila* larvae leads to chromosomal abnormalities and  
70 genomic instability [27]. Depletion of the Arp2/3 complex in human cells additionally results in  
71 defects in DNA damage-induced apoptosis [29].

72         Apart from their functions in chromatin-associated processes during interphase, actin  
73 and its nucleators, especially Formins and the Arp2/3 complex, are increasingly being found to  
74 support proper chromosome movements during meiosis and mitosis. In starfish oocytes,  
75 following nuclear envelope breakdown, several types of F-actin structures promote chromosome  
76 transport and coordinate capture by microtubules [30,31]. Studies in mouse oocytes further  
77 indicate that actin filaments permeate the meiotic microtubule spindles and facilitate proper  
78 chromosome congression [32,33]. Chemical inhibition of actin dynamics or genetic inactivation  
79 of Formin-2 prevents proper formation of kinetochore microtubules and leads to chromosome  
80 alignment and segregation errors [33,34]. Similarly, during mitosis, several actin structures  
81 have been shown to interact with and possibly guide microtubule spindle components. Actin  
82 filaments that run between the microtubule spindle poles and F-actin fingers that project from  
83 the cell cortex into the spindle have been identified in *Xenopus* epithelial cells [35].  
84 Centrosomes, which serve as major microtubule nucleation and organizing centers, are also  
85 sites of actin assembly [36]. The Arp2/3 complex localizes to centrosomes in multiple  
86 mammalian cell types, and pharmacological inhibition of Arp2/3 results in decreased  
87 centrosomal actin levels and impaired mitotic spindle formation [37-39]. Thus, disruption of  
88 either actin or Arp2/3 function during meiosis or mitosis can lead to defects in chromosome  
89 dynamics, highlighting the actin cytoskeleton as a key player in maintaining genomic integrity  
90 during nuclear division.

91         Although the effects of transient Arp2/3 depletion or inhibition on chromatin repair are  
92 now evident, and several aberrations in chromosome movement have been characterized, the  
93 impact of total and permanent Arp2/3 ablation on these processes has not been established.  
94 The development of several cellular systems for studying long-term Arp2/3 depletion or deletion

95 has allowed more clear-cut assessments of the requirements for the Arp2/3 complex in a given  
96 cellular process [14,40-43]. For example, these models have already provided fundamental  
97 insights into the function of the Arp2/3 complex in cell migration. Studies using mouse  
98 embryonic fibroblasts (MEFs) expressing shRNAs targeting the ArpC2 and Arp2 subunits [40],  
99 embryonic stem cell-derived mouse fibroblasts lacking the ArpC3 subunit [14], and mouse  
100 fibroblasts harboring a tamoxifen-inducible knockout of the Arp3 subunit [43], indicate that the  
101 Arp2/3 complex is crucial for lamellipodia formation and directional migration. Additionally,  
102 mouse fibroblasts containing a tamoxifen-inducible knockout of the ArpC2 subunit exhibit  
103 impaired lamellipodia formation and reduced motility speeds [42].

104 To determine the outcome of Arp2/3 complex ablation on chromatin-associated  
105 processes related to cell viability and multiplication, we employed the inducible ArpC2 knockout  
106 cell model [42]. Our findings establish a key connection between Arp2/3 complex functions in  
107 genomic integrity during interphase and mitosis in normal cells to the biogenesis of micronuclei  
108 and induction of a cellular senescence pathway upon Arp2/3 inactivation.

## 109 **Results**

### 110 **ArpC2 iKO cells undergo an abrupt proliferation arrest and morphological enlargement**

111 Given that the Arp2/3 complex is required for viability in many eukaryotic organisms, we sought  
112 to better understand its essential nature – apart from its well-recognized roles in adhesion and  
113 motility – in mammalian cells. The Arp2/3 complex is composed of seven subunits: two Actin-  
114 related proteins (Arp2 and Arp3) and five Complex subunits (ArpC1-C5), with ArpC2 and ArpC4  
115 forming a structural core and multiple isoforms of Arp3, ArpC1, and ArpC5 providing peripheral  
116 diversity [4,44]. Previous work indicates that MEFs subjected to RNAi-mediated depletion of the  
117 ArpC2 and Arp2 subunits are viable and remain culturable when generated in a genetic  
118 background lacking the *p16Ink4a/Arf* tumor suppressors [40]. More recently, to circumvent  
119 problems with knockdown instability, a conditional knockout model was created using  
120 *p16Ink4a/Arf*<sup>-/-</sup> mouse tail fibroblasts (MTFs) harboring a floxed *ArpC2* allele and engineered to  
121 express the CreER recombinase upon treatment with 4-hydroxytamoxifen (4-OHT) [42]. Since  
122 the latter system is inducible, causes a permanent loss of the critical ArpC2 subunit, and leads  
123 to degradation of other members of the complex, we adopted this Arp2/3 complex null cellular  
124 model for our studies. In all of our experiments, parental MTFs carrying the conditional *ArpC2*  
125 allele were exposed to DMSO to maintain a control (Flox) cell population or to 4-OHT to  
126 generate ArpC2 induced knockout (iKO) cells.

127 For initially assessing the kinetics of Arp2/3 complex depletion, DMSO- and 4-OHT-  
128 treated cells were collected at various timepoints, lysed, and immunoblotted with antibodies to  
129 the ArpC2 and Arp3 subunits plus antibodies to GAPDH and tubulin as loading controls (Fig  
130 1A). After 1 day in 4-OHT, ArpC2 protein levels were reduced by nearly half compared to  
131 DMSO-treated Flox cells (Fig 1A and 1B). By 2 days, ArpC2 expression was diminished by  
132 approximately 80%, and a reduction in Arp3 levels became noticeable (Fig 1A and 1B). The  
133 amounts of both subunits continued to steadily decline in the iKO cells over time until they were

134 absent following 5 days in 4-OHT (Fig 1A and 1B). DMSO and 4-OHT were removed from  
135 culture media after 6 days, but ArpC2 and Arp3 remained undetectable in the iKO population  
136 out to 13 days (Fig 1A and 1B). To independently confirm the loss of the Arp2/3 complex by  
137 fluorescence microscopy, Flox and iKO cells were stained with an antibody to label Arp3 and  
138 with fluorescent phalloidin to visualize F-actin. As expected, Flox cells exhibited prominent Arp3  
139 staining within F-actin-rich peripheral membrane ruffles, whereas Arp3 staining and ruffles were  
140 both missing from the iKO cells (Fig 1C). Collectively, these results demonstrate that in this  
141 cellular context, the Arp2/3 complex knockout is rapid, complete, and stable over time.

142 To determine the impact of abolishing Arp2/3 complex expression on cell proliferation,  
143 we next quantified cell titers on a daily basis following the addition of DMSO or 4-OHT. For the  
144 first 3 days, Flox and iKO cells multiplied at identical rates, but by 4 days, the growth  
145 characteristics of Flox and iKO cultures began to diverge, and at 5 days, the iKO samples were  
146 proliferating at a clearly slower pace (Fig 1D). After approximately 10-12 days, virtually all iKO  
147 cells stopped dividing (Fig 1D). To quantify the differences in cell multiplication rates, we  
148 calculated the population doubling times in the 0-4 and 5-12 day time periods following DMSO  
149 or 4-OHT exposure. While the doubling times were similar for Flox and iKO populations (18h  
150 vs. 20h) during the first interval, the iKO doubling times quadrupled to >80h in the 5-12 day  
151 range (Fig 1E). Moreover, cell counts in iKO samples remained unchanged for an additional  
152 week (Fig 1D), except in instances where colonies of 4-OHT escapees or revertants re-  
153 expressing the Arp2/3 complex emerged (not depicted). Consistent with a requirement for the  
154 Arp2/3 complex in intrinsic apoptosis [29], apoptotic cell phenotypes were not observed in the  
155 iKO cell population. Thus, following loss of the Arp2/3 complex, MTF cells undergo an abrupt  
156 and stable proliferation arrest.

157 When examining the different growth characteristics of the Flox and iKO cultures, it also  
158 became apparent that the two cell types had distinct morphologies and sizes. Fluorescent  
159 phalloidin staining, in addition to revealing a lack of F-actin-rich ruffles (Fig 1C), demonstrated



160 that iKO cells were flatter and larger than Flox cells (Fig 1F). Quantification of Flox and iKO cell  
161 areas showed that the iKO cells were, on average, about twice as large as Flox cells (Fig 1G).  
162 So in addition to losing their ability to multiply, Arp2/3-deficient cells display significant increases  
163 in their size.

164

### 165 **ArpC2 iKO cells exhibit the canonical nuclear and cytoplasmic features of senescence**

166 A loss of proliferative capacity and an increase in adherent cell area are common characteristics  
167 of senescent cells. Cellular senescence refers to a permanent state of replicative arrest [45,46],  
168 and is reflected in several additional physiological changes, including increased production of  
169 pro-inflammatory proteins, a response known as the senescence-associated secretory  
170 phenotype, or SASP [47,48]. Notably, previous global gene expression profiling using the  
171 ArpC2/Arp2-depleted MEF model revealed that several genes common to the SASP were up-  
172 regulated [41], suggesting a link between the loss of Arp2/3 function and this aspect of cellular  
173 senescence. To investigate whether the ArpC2 iKO cells also displayed this senescence  
174 feature, we performed RT-PCR (Fig 2A) and RT-qPCR (Fig 2B) to compare transcript levels for  
175 Interleukin-6 (Il-6), a pro-inflammatory cytokine consistently present in the SASPs derived from  
176 senescent cells with diverse origins [49,50]. In agreement with findings from the ArpC2/Arp2  
177 RNAi MEF studies, *Il-6* expression was greater in iKO cells than in Flox cells at 3, 6, and 9 days  
178 after the onset of 4-OHT treatment (Fig 2A). RT-qPCR revealed that *Il-6* transcript levels were  
179 nearly 4-fold higher in the iKO compared to Flox cells at 9 days (Fig 2B), indicating that a  
180 permanent loss of the Arp2/3 complex induces the production of this key SASP component.

181 Senescence is also frequently associated with changes in nuclear structure, including  
182 decreased levels of Lamin B1, a structural protein of the nuclear lamina [51]. To determine if  
183 Lamin B1 abundance was altered by the deletion of ArpC2, we immunoblotted Flox and iKO  
184 cells for Lamin B1 and found that Lamin B1 protein levels were indeed 3-fold lower in iKO cell  
185 populations (Fig 2C and 2D). To confirm the reduction in Lamin B1 expression, Flox and iKO

186 cells were also subjected to immunofluorescence microscopy. In Flox cells, nuclear Lamin B1  
187 staining was consistently bright (Fig 2E and 2F). Contrastingly, in iKO cells, nuclear Lamin B1  
188 levels were visibly lower (Fig 2E and 2F). In agreement with the immunoblotting data,  
189 quantification of nuclear fluorescence intensities demonstrated that, on average, Lamin B1 was  
190 nearly 3-fold less abundant in iKO cells (Fig 2F).

191 In addition to the production of a transcriptional SASP response and a decrease in their  
192 nuclear Lamin B1 levels, senescent cells typically exhibit a cytoplasmic senescence-associated  
193  $\beta$ -galactosidase (SA- $\beta$ gal) activity at pH 6 [52]. This is the most widely accepted biomarker of  
194 senescence. SA- $\beta$ gal staining in Flox and iKO cells from 0-22 days revealed that by 7 days,  
195 and at later timepoints, the number of SA- $\beta$ gal-positive cells was significantly higher in iKO than  
196 Flox populations (Fig 3A and 3B). In many instances, SA- $\beta$ gal activity is thought to reflect an  
197 increase in lysosomal content [53,54]. So to assess lysosomal abundance, we treated Flox and  
198 iKO cells with LysoTracker, a fluorescent probe that labels acidic intracellular structures, and  
199 examined the cells microscopically. LysoTracker intensely stained discrete circular puncta  
200 resembling lysosomes in Flox cells, but broadly stained large portions of the cytoplasm in iKO  
201 cells (Fig 3C). Quantification of LysoTracker fluorescence at day 9 revealed that more than  
202 80% of iKO cells versus 5% of Flox cells showed the more expansive staining pattern (Fig 3D).  
203 Furthermore, >10% of the areas within iKO cells stained positive for LysoTracker compared to  
204 <1% of the areas in Flox cells (Fig 3D). Thus, the arrest, morphological, and SASP  
205 observations, when taken together with these Lamin B1, SA- $\beta$ gal, and LysoTracker staining  
206 results, establish that ArpC2 iKO cells undergo senescence.

207

### 208 **The formation of micronuclei and DNA damage clusters precedes iKO cell senescence**

209 Cellular senescence can be induced by a variety of stimuli, including DNA damage, oncogene  
210 activation, telomere shortening, and mitochondrial dysfunction [55-57]. Micronuclei and  
211 cytosolic chromatin fragments are common senescence-associated phenotypic traits and

212 influence the senescent state [58-60]. During the course of our characterization of the  
213 senescence parameters described above, we noticed that iKO cells frequently contained  
214 micronuclei whereas Flox cells did not (Fig 1C; Fig 2E; Fig 3C). Following specific examinations  
215 of samples containing DAPI-stained DNA, it became obvious that small cytosolic micronuclei  
216 were often present in iKO cells (Fig 4A). Of iKO cells with micronuclei, most had one  
217 micronucleus (Fig 4B; i, ii, iii), but some harbored 2 or 3 micronuclei (Fig 4B; iv, v, vi).  
218 Micronuclei ranged in size and could be found completely detached (Fig 4B; i, ii, vi) or tethered  
219 to the periphery (Fig 4B; iii, iv, v) of the main nucleus. We next quantified the timing and  
220 frequency with which micronuclei formed in Flox and iKO cells. Surprisingly, after just one day  
221 in 4-OHT, about 13% of iKO cells had micronuclei (Fig 4C). The percentage of iKO cells with  
222 micronuclei plateaued at approximately 20% by 3 days and remained steady out to 13 days,  
223 whereas the proportion of Flox cells with micronuclei stayed at around 5% throughout the entire  
224 time course (Fig 4C). Therefore, a notably rapid formation of micronuclei precedes the  
225 proliferation arrest and SA- $\beta$ gal positivity that results from *ArpC2* inactivation.

226         Since micronuclei are often indicative of genomic instability, we next assessed the extent  
227 of DNA damage in Flox and iKO cells. Staining with an antibody to the modified histone protein  
228 H2AX ( $\gamma$ H2AX), which is phosphorylated in response to double-stranded DNA breaks [61],  
229 demonstrated that iKO cells contained prominent DNA damage clusters in their nuclei and  
230 micronuclei (Fig 5A). Upon closer inspection, Flox cells typically exhibited no or diffuse  $\gamma$ H2AX  
231 staining in their nuclei (Fig 5B), whereas iKO cells frequently had 1-3 isolated  $\gamma$ H2AX clusters  
232 that localized to the nuclear periphery and/or within micronuclei (Fig 5B). Quantification of the  
233 percentage of cells with  $\gamma$ H2AX clusters following the addition of DMSO or 4-OHT revealed that  
234 clusters began to increase in iKO cells by 2 days, and that from 3 days onward, clusters were  
235 significantly more common in iKO cells than in Flox cells (Fig 5C). The fraction of iKO cells with  
236  $\gamma$ H2AX clusters leveled out at approximately 25%, while the proportion of Flox cells containing  
237 clusters was always 3-6% (Fig 5C). These results are consistent with previous observations in

238 which *Drosophila* and mouse cells exposed to ionizing radiation and subjected to RNAi-  
239 mediated Arp2/3 depletion were found to contain DNA damage and micronuclei [27]. However,  
240 our results indicate that even without exposure to acute genotoxic agents, losing the Arp2/3  
241 complex can cause an accumulation of damaged DNA elements that incorporate into  
242 micronuclei, thereby illustrating that the Arp2/3 complex is a crucial player in maintaining  
243 genomic integrity under relatively normal cell culture conditions.

244

#### 245 **Activation of p53 and upregulation of *Cdkn1a/p21* accompany the ArpC2 iKO cell arrest**

246 In light of the biogenesis of  $\gamma$ H2AX clusters and micronuclei, we hypothesized that a DNA  
247 damage response might be activated in the ArpC2 iKO cells. To explore this possibility, we  
248 immunoblotted Flox and iKO cell extracts with antibodies to the crucial tumor suppressor protein  
249 and transcription factor p53, which typically becomes stabilized, phosphorylated, and enriched  
250 in the nucleus following DNA damage [62,63]. Consistent with this expectation, by 3 days after  
251 4-OHT vs DMSO treatment, p53 levels were higher in iKO than in Flox cells, and p53 was  
252 phosphorylated on Serine-15 (Fig 6A). Furthermore, immunofluorescence microscopy revealed  
253 that nuclear p53 fluorescence was more intense in iKO cells than in Flox cells (Fig 6B). These  
254 results imply that a p53-mediated DNA damage response is induced in Arp2/3-depleted cells.

255 Two of the major factors involved in the cell cycle arrest that leads to senescence are  
256 the cyclin-dependent kinase inhibitors *Cdkn2a/p16INK4A* (p16) and *Cdkn1a/p21CIP/WAF* (p21).  
257 Elevated levels of both of these anti-proliferative transcripts/proteins are frequently used as  
258 indicators of the senescent state [55,64], although populations of cells expressing high levels of  
259 p16 appear to be distinct from those expressing high levels of p21, at least in tissues from aged  
260 mice [65]. Since p21 is a known transcriptional target of p53 [66,67], and the MTFs used in our  
261 studies lack p16, we postulated that *Cdkn1a/p21* was associated with the onset of senescence  
262 in the iKO cells. To test this, we performed RT-PCR (Fig 6C) and RT-qPCR (Fig 6D) to  
263 compare *Cdkn1a* transcript levels in Flox and iKO cells over a 9-day time period. Indeed,

264 *Cdkn1a* expression appeared greater in the iKO cells than in the Flox cells at 6 and 9 days after  
265 the initiation of 4-OHT treatment (Fig 6C). RT-qPCR revealed that *Cdkn1a* transcript levels  
266 were doubled in the iKO cells relative to the Flox cells at 9 days (Fig 6D), showing that deletion  
267 of the Arp2/3 complex leads to an upregulation of this key cell cycle regulator. To evaluate  
268 whether the increase in *Cdkn1a* transcript corresponded to greater p21 protein levels, Flox and  
269 iKO cells were treated with antibodies to p21 and subjected to immunofluorescence microscopy  
270 (Fig 6E). Quantification of p21 nuclear intensity at the 6 day timepoint verified that p21 levels  
271 were significantly higher in iKO than in Flox cells (Fig 6E and 6F). Together, the p53  
272 enrichment and p21 upregulation in iKO cells support the idea that a DNA damage response  
273 signaling pathway accompanies cell cycle arrest after the Arp2/3 complex is removed.

274

#### 275 **Cytoplasmic cGAS and STING are recruited to micronuclei**

276 In addition to the above nuclear changes that took place upon Arp2/3 ablation, it seemed likely  
277 that cytoplasmic changes arising from the presence of micronuclei in ArpC2 iKO cells would  
278 also be linked to the onset of senescence. We hypothesized that a cytosolic DNA detection and  
279 signaling pathway involving the cyclic GMP-AMP Synthase (cGAS) enzyme, which recognizes  
280 extra-nuclear chromatin and relays a signal to the downstream effector molecule STING [60,  
281 68,69], might also be activated in iKO cells. Tagged cGAS can be recruited to micronuclei, and  
282 through its detection of cytosolic DNA and activation of STING, promotes pro-senescence and  
283 pro-inflammatory gene expression [70-72]. To determine if tagged cGAS localizes to the  
284 micronuclei in ArpC2 iKO cells, we transiently transfected MTFs with plasmids encoding  
285 mCherry-cGAS or mCherry as a control (Fig 7A), and treated them with 4-OHT to induce *ArpC2*  
286 deletion. mCherry was highly expressed in the iKO cells but was not recruited to micronuclei  
287 (Fig 7B). In contrast, mCherry-cGAS showed intense localization to micronuclei (Fig 7B),  
288 indicating that it can detect the cytosolic DNA in iKO cells.

289 We next wanted to determine the localization of endogenous cGAS and STING in the

290 MTFs. Immunoblotting indicated that cGAS and STING were expressed at similar levels in Flox  
291 and iKO cells (Fig 7C), so to test whether cGAS and/or STING were recruited to the  
292 micronuclei, we visualized these proteins via immunofluorescence microscopy after 3-4 days,  
293 when micronuclei become more abundant in iKO cells and just before Flox and iKO  
294 multiplication rates begin to diverge. Consistent with previous studies [73,74], endogenous  
295 cGAS was present in the nuclei of both Flox and iKO cells (Fig 7D). It was also readily apparent  
296 in nearly 40% of iKO cell micronuclei (Fig 7D). The rare micronuclei that formed in Flox cells  
297 also recruited cGAS (Fig 7D magnification). For STING, an integral membrane protein that  
298 localizes to organelles of the conventional secretory pathway, including the endoplasmic  
299 reticulum (ER) and Golgi [75], immunofluorescence revealed a speckled ER-like localization in  
300 both Flox and iKO cells, and enrichment around micronuclei (Fig 7D inset). Immunolabeling for  
301 STING, the ER chaperone GRP94, and the *cis*-Golgi protein GM130 implied that ER and not  
302 Golgi membranes are more likely to surround subsets of micronuclei in iKO cells (Fig 7E).  
303 These findings are consistent with a function for cGAS in recognizing damaged DNA in the  
304 cytosol and initiating a signaling pathway that locally activates STING near micronuclei in  
305 Arp2/3-deficient cells.

306 To explore whether cGAS affects the cell proliferation arrest that takes place when the  
307 Arp2/3 complex is lost, MTFs were exposed to 4-OHT for 3 days to induce the deletion of *ArpC2*  
308 and then transferred into media containing the cGAS inhibitor RU.521 [76] or DMSO as a  
309 control. Quantification of cell replication rates during days 4-6 following the onset of 4-OHT  
310 treatment revealed that RU.521 caused a modest but statistically faster population doubling time  
311 in the iKO cells (Fig 7F), implying that cGAS inhibition has the potential to oppose the initiation  
312 of senescence in some of the cells in this experimental system. Collectively, the above  
313 localization and inhibitor results support the idea that cGAS/STING signaling contributes to the  
314 establishment of senescence in Arp2/3-deficient cells.

315

316 **Micronuclei form as a result of mitotic defects in ArpC2 iKO cells**

317 Because ArpC2 iKO cells accumulate DNA damage, form micronuclei with high frequency, and  
318 undergo senescence in a p53/p21- and cGAS/STING-associated manner, we next wanted to  
319 determine how this critical process of micronucleus biogenesis takes place. Micronuclei can  
320 form as a result of chromosome missegregation during mitosis and from expulsion of damaged  
321 DNA from the nucleus during interphase [58,77-80]. To differentiate between the possibilities  
322 that micronuclei are a product of defects in mitosis versus aberrant nuclear remodeling in  
323 interphase, we expressed the GFP-tagged histone H2B in MTFs and visualized chromatin  
324 dynamics in live cells. These experiments were performed within the first 2 days of DMSO or 4-  
325 OHT treatment, when Arp2/3 complex levels were declining the fastest (Fig 1B), the cells were  
326 still dividing rapidly (Fig 1E), and the incidence of micronucleus formation was highest (Fig 4C).

327 Timelapse imaging of H2B-GFP-expressing Flox cells revealed that the majority of  
328 mitoses resulted in an equal partitioning of nuclear chromatin into two daughter cells (Fig 8A).  
329 However, iKO cell mitoses often yielded micronuclei due to errors in chromatin segregation (Fig  
330 8A). This was repeatedly observed when chromatin fragments near the metaphase plate were  
331 not properly distributed to daughters during anaphase (Fig 8A). Another common phenotype of  
332 iKO cells that entered mitosis was premature mitotic exit (Fig 8B). Such cells underwent a  
333 prolonged prometaphase or metaphase, failed to enter anaphase, and ultimately returned to  
334 interphase with nuclei containing twice their normal chromatin content (Fig 8B). Micronuclei  
335 also formed in some of these cells that failed to complete mitosis (Fig 8B).

336 We next measured the frequencies with which the mitotic defects occurred. First,  
337 approximately 23% of completed mitoses in iKO cells yielded micronuclei compared to only  
338 about 6% of completed mitoses in Flox cells (Fig 8C). Second, after categorizing the stages of  
339 mitosis and determining the number of timelapse frames spent specifically in metaphase  
340 (judged by the presence of at least 95% of H2B-GFP fluorescence aligned compactly at the cell  
341 equator), we found that >80% of Flox cells that completed mitosis spent only one frame in



342 metaphase, whereas only 40% of iKO cells proceeded through metaphase with this speed (Fig  
343 8D). The other 60% of iKO cells that completed mitosis spent two or more frames in metaphase  
344 (Fig 8D), suggesting that iKO cells experience an unusually prolonged metaphase period.  
345 Third, when evaluating the incidence of premature mitotic exits (defined as cells that entered  
346 prophase but did not complete anaphase), we discovered that nearly 30% of iKO cells that  
347 entered prophase underwent premature mitotic exits compared to only 10% of Flox cells (Fig  
348 8E). Approximately 14% of premature mitotic exits that took place in the iKO cells also gave  
349 rise to micronuclei. Fourth, among the 330 iKO interphase nuclei that were observed during live  
350 cell imaging, at most 2 (i.e.,  $\leq 0.6\%$ ) appeared to create micronuclei via budding or extrusion,  
351 indicating that micronuclei form almost exclusively during mitosis. As a final point, to confirm  
352 that the prevalent chromatin missegregation events in iKO cells were, at least in part,  
353 attributable to the presence of broken DNA fragments, we fixed and stained mitotic cells for  
354  $\gamma$ H2AX. In agreement with this possibility, during prometaphase and metaphase, iKO cells  
355 contained  $\gamma$ H2AX foci at the periphery of or completely detached from the main chromatin mass  
356 (Fig 8F). Furthermore, in early anaphase, iKO cells displayed prominent DNA damage clusters  
357 near their equators, and by late anaphase,  $\gamma$ H2AX-positive lagging chromosomes became  
358 apparent (Fig 8F). Overall, these live and fixed cell studies show that, during Arp2/3-depleted  
359 conditions, damaged chromatin fragments persist and are incorporated into micronuclei as a  
360 result of defects in mitotic chromosome segregation.

361

### 362 **Actin filament penetration into the central spindle is diminished in Arp2/3-depleted cells**

363 Upon discovering that knocking out the Arp2/3 complex leads to chromatin partitioning defects,  
364 we wanted to also assess how the loss of this actin nucleator might alter the actin and  
365 microtubule cytoskeletons during mitosis. Actin has been observed in various parts of meiotic  
366 and mitotic spindles in diverse organisms [30-39], so to examine the organization and intensity  
367 of actin filaments in relation to microtubule spindles in MTFs, we stained mitotic Flox and iKO



368 cells with phalloidin to label F-actin, an anti-tubulin antibody to visualize microtubules, and DAPI  
369 to detect DNA. We focused on metaphase, when the chromosomes are either properly or  
370 improperly aligned at the central spindle, corresponding to when Flox mitoses rapidly proceed or  
371 iKO mitoses frequently stall. Imaging of metaphase Flox cells in multiple focal planes revealed  
372 that several distinct F-actin structures were present. In the lower portions of cells, linear actin  
373 filaments in the shape of a spindle and several bundles of microtubules were observed (Fig 9A).  
374 In the middle planes of cells, multiple thick finger-like F-actin structures penetrated the  
375 chromosomal region, and numerous microtubules comprising the main microtubule spindle were  
376 apparent (Fig 9A). In the upper parts of cells, fewer F-actin and microtubule structures  
377 intercalated the central spindle area (Fig 9A). Staining with anti-ArpC2 antibodies indicated that  
378 the Arp2/3 complex was not enriched along the thin linear actin filaments at the lower part of the  
379 cell, but was present near F-actin and microtubules in the middle and upper spindle structures  
380 (Fig 9A). Together, these observations expand the catalog of F-actin and Arp2/3-associated  
381 cytoskeletal structures that are found within dividing mammalian cells.

382 For more closely examining the spatial positioning of actin filaments, microtubules, and  
383 the Arp2/3 complex at the metaphase plate, we performed fluorescence intensity line scan  
384 analyses through the chromatin-containing region. Peaks of spindle microtubule intensity often  
385 coincided with peaks of F-actin intensity as well as sites of ArpC2 enrichment (Fig 9B). In  
386 contrast, DNA staining levels were highest where microtubules and F-actin were lowest (Fig  
387 9B). These observations show a positive relationship between F-actin and microtubule  
388 localization in the central metaphase spindle.

389 To determine whether loss of the Arp2/3 complex causes any abnormalities in F-actin  
390 organization during metaphase, we compared F-actin staining in Flox and iKO cells. Actin  
391 filament levels in the metaphase chromatin-containing region appeared less prominent in iKO  
392 cells than in Flox cells (Fig 9C). Quantification of phalloidin fluorescence intensities in these  
393 regions of the central spindle revealed that F-actin levels were significantly lower in iKO cells

394 compared to Flox cells (Fig 9D). This was not due to a general deficit in central spindle staining,  
395 because the fluorescence intensity of microtubules in the same region was not significantly  
396 different between iKO and Flox cells (Fig 9D). A reduction in the penetration of actin filaments,  
397 but not microtubules, into the metaphase chromatin-containing region of iKO cells was further  
398 reflected by fewer prominent F-actin peaks in fluorescence intensity plot profiles (Fig 9E).  
399 Collectively, these results indicate that a functional Arp2/3 complex is required for the  
400 polymerization of actin filaments in the vicinity of metaphase chromosomes.

401

### 402 **Arp2/3 depletion results in anaphase microtubule asymmetry**

403 Since metaphase spindle-associated F-actin overlapped with microtubules in Flox cells and was  
404 less prominent in Arp2/3 knockout cells, we considered that the subsequent arrangement of  
405 microtubules during chromosome segregation might be altered. To explore this possibility, we  
406 evaluated microtubule organization and intensity during anaphase, when the chromosomes are  
407 either correctly or incorrectly partitioned. Flox cells exhibited uniform distributions of  
408 microtubules across the width of the separating spindle (Fig 10A), as evidenced by the relatively  
409 evenly-spaced peaks in fluorescence intensity plots perpendicular to the presumed position of  
410 the cytokinetic ring (Fig 10B). In contrast, iKO cells displayed unbalanced tubulin intensities in  
411 which the microtubules appeared to be more heavily concentrated on one side of the spindle  
412 (Fig 10A and 10B). These results suggest that in addition to the presence of misplaced  
413 damaged chromatin and a decrease in actin filaments at the metaphase plate, chromosome  
414 missegregations arising from alterations in anaphase microtubule organization may be a  
415 contributing factor in the formation of micronuclei in Arp2/3-deficient cells. Thus, loss of the  
416 Arp2/3 complex has multiple significant molecular consequences – beginning with unrepaired  
417 DNA damage and including mitotic actin and microtubule cytoskeleton abnormalities – that lead  
418 to a p53/p21 response, the biogenesis of micronuclei, cGAS/STING recruitment, and the onset  
419 of senescence.

## 420 **Discussion**

421 The Arp2/3 complex is a key driver of many cellular processes that are mediated by actin  
422 assembly at the plasma membrane, namely adhesion, endocytosis, protrusion, and migration.  
423 While the complex is evolutionarily conserved among nearly all eukaryotes and is essential for  
424 viability in animals, the molecular basis underlying its indispensability is unclear. Roles for the  
425 Arp2/3 complex in enabling DNA repair during interphase, promoting chromosome partitioning  
426 during meiosis/mitosis, and controlling apoptosis following DNA damage have recently emerged  
427 and may help explain why Arp2/3 is essential. Such studies prompted us to determine the  
428 effects of permanent Arp2/3 complex ablation on viability, proliferation, and chromatin-  
429 associated processes in mammalian cells. Our results reveal important functions for the Arp2/3  
430 complex in maintaining genomic integrity and supporting mitotic progression, while uncovering  
431 striking mechanistic connections between actin cytoskeleton defects and senescence.

432 Various endogenous stresses are known to induce cellular senescence, including  
433 replicative, telomeric, genotoxic, oncogenic, oxidative, and mitochondrial stress [81]. Our  
434 studies now add cytoskeletal dysfunction as a trigger of senescence. Arp2/3 complex knockout  
435 cells, in addition to a stable proliferation arrest and physical enlargement, display multiple  
436 phenotypic hallmarks of senescence. These include an increase in *p16* transcript reflective of  
437 SASP expression and a reduction of nuclear Lamin B1 levels. The iKO cells also harbor high  
438 cytoplasmic SA- $\beta$ gal activity and increased acidic organelle content. Given that the Arp2/3  
439 complex influences most cellular functions, from plasma membrane remodeling [2,15,82] to  
440 mitochondrial dynamics [83] to autophagy [84] to DNA repair [27,28], it seems likely that multiple  
441 intracellular defects derived from Arp2/3 deficiency can impact senescence induction. Potential  
442 changes in mitochondrial turnover, combined with altered lysosomal content could signify  
443 increases in mitochondrial, oxidative, and proteotoxic stress in iKO cells. The extent to which  
444 these stressors contribute to the initiation or maintenance of senescence will be an important

445 area of future investigation.

446 Despite uncertainties in the severity of cytoplasmic organelle dysfunction in iKO cells,  
447 obvious defects in nuclear and chromatin-associated processes emerged as major factors in  
448 promoting senescence in our studies. Kinetic analyses indicate that 1-3 days after exposure to  
449 4-OHT, ArpC2 (and thus functional Arp2/3 complex) levels are 50-90% depleted (Fig 1A and  
450 1B). This time period coincides with the steepest increases in detection of micronuclei via DAPI  
451 staining (Fig 4C) and visualization of dsDNA breaks in both nuclei and micronuclei via  $\gamma$ H2AX  
452 staining (Fig 5C). A DNA damage response is activated, as evidenced by increased p53  
453 expression and phosphorylation (Fig 6A and 6B). By 4-6 days, the p53-regulated cell cycle  
454 inhibitor p21 accumulates in the nucleus (Fig 6C-F) and cell multiplication stops (Fig 1D). By 7  
455 days, SA- $\beta$ gal-positivity begins to increase (Fig 3A and 3B). At 7-10 days, the entire population  
456 of iKO cells appears to be senescent, given the complete lack of proliferation (Fig 1D), as well  
457 as consistent single cell phenotypes in enlargement (Fig 1G), nuclear Lamin B1 reduction (Fig  
458 2F), and cytoplasmic acidity (Fig 3D). Beyond 10 days, the iKO cell population remains viable  
459 but non-replicative while maintaining 20-25% positivity for micronuclei and SA- $\beta$ gal activity.

460 While it is clear that all Arp2/3 knockout cells senesce, it is unclear why only a fraction of  
461 the culture is SA- $\beta$ gal positive. This could be a technical matter of assay sensitivity, or intense  
462 SA- $\beta$ gal-positivity may simply develop later in some cells. Additionally, the reasons why the  
463 entire culture senesces when only a quarter of the iKO cells harbor detectable micronuclei  
464 remain ambiguous. It is conceivable that aneuploidy as a result of receiving insufficient  
465 chromatin following mitosis or from excess DNA content following premature mitotic exits  
466 contributes to a p53-mediated arrest program in micronucleus-negative cells. Another  
467 possibility is that paracrine signaling from mature senescent cells to others in the culture  
468 supports the global proliferation block.

469 In response to damaging stimuli, the cyclin-dependent kinase inhibitors p16 and p21 are

470 frequently upregulated and act as key players in pathways that promote the replicative arrest  
471 that defines senescence [55-57]. Earlier studies showed that inactivation of *p16Ink4a/Arf* is  
472 necessary for establishing Arp2/3-depleted mouse fibroblast cultures, suggesting that the loss of  
473 Arp2/3 can induce growth arrest or death in a p16-mediated manner [40,41]. More recent  
474 experiments in human cells treated with a genotoxic agent indicate that depletion of the Arp2/3  
475 complex or inactivation of two of its upstream regulators prevents the execution of apoptosis  
476 [29]. Such cells undergo a p53- and p21-associated cell cycle arrest but fail to properly  
477 complete an apoptosome-based caspase cleavage cascade [29]. These observations, together  
478 with our data showing that ArpC2 iKO cells activate p53 and accumulate p21 in a p16-  
479 independent manner, suggest that losing the Arp2/3 complex can trigger multiple cell cycle  
480 arrest pathways. While p53 is known to cause upregulation of *Cdkn1a/p21* to promote arrest  
481 [85-87], deciphering the degree to which other anti-proliferative mechanisms cooperate with p21  
482 in iKO cells requires more investigation. Interestingly, studies in aged mice show that cells  
483 expressing high levels of p21 are mostly distinct from those expressing high levels of p16 [65],  
484 further highlighting the possibility that loss of the Arp2/3 complex *in vivo* may instigate different  
485 pathways to senescence depending on the physiological state of the cell and its tissue of origin.

486 In addition to the functions of p53 and p21 in the nucleus, it seems likely that recognition  
487 of micronuclei in the cytoplasm also participates in the senescence response in Arp2/3-deficient  
488 cells. We observed cGAS and STING localization at or around micronuclei in ArpC2 iKO cells,  
489 and a chemical inhibitor of cGAS seemed to slightly increase multiplication of iKO cultures.  
490 Recent work has also implicated cGAS/STING in regulating p21 expression, as depletion of  
491 cGAS or STING results in reduced p21 levels and premature mitotic entry [88]. These results  
492 support the notion that multiple nuclear and cytoplasmic signaling factors contribute to the  
493 induction and maintenance of the proliferation arrest in ArpC2 iKO cells.

494 The main mechanism underlying micronucleus biogenesis in Arp2/3-deficient cells is a  
495 lack of fidelity in chromatin partitioning during mitosis, as revealed by our live imaging studies.

496 Such segregation defects can be primarily explained by broken DNA fragments failing to  
497 properly attach to the microtubule spindle, since most micronuclei formed from cells completing  
498 inaccurate mitoses. However, cytoskeletal abnormalities may also contribute to chromosome  
499 segregation errors, as changes in the organization of metaphase F-actin and anaphase  
500 microtubules are also prevalent in the knockout cells. Our findings complement previous  
501 experiments showing altered F-actin levels in meiotic/mitotic structures and defects in spindle  
502 formation following chemical inhibition of Arp2/3 [37-39]. Interestingly, many mitoses in ArpC2  
503 iKO cells feature a prolonged metaphase period. Delayed mitoses arising from failure to satisfy  
504 spindle assembly checkpoints can cause chromosome segregation mistakes and premature  
505 mitotic exits, both of which give rise to aneuploid cells [89], and both of which were observed at  
506 high frequencies in iKO cells. Thus, Arp2/3 complex deficiency leads to multiple deleterious  
507 consequences in M-phase of the cell cycle. More work is needed to determine how Arp2/3,  
508 actin, and microtubules collaborate in controlling spindle positioning, chromosome alignment,  
509 and DNA segregation.

510         Given that high mutation rates and aneuploidy are associated with organismal aging and  
511 tumorigenesis [90], impairment of Arp2/3 function *in vivo* could be a contributor to the  
512 development of age-related dysfunction and cancers. One central feature of the aging process  
513 is an accumulation of senescent cells, which can drive several aging phenotypes [91,92]. Such  
514 discoveries have led to the development of new “senolytic” classes of drugs to treat and slow  
515 the progression of age-related pathologies [93]. Our findings suggest that impaired Arp2/3  
516 complex function, and potentially other actin cytoskeletal misregulation, may contribute to  
517 premature senescence and aging. Taken together with previous observations that F-actin  
518 integrity affects aging and lifespan in *C.elegans* [94,95], preventing or correcting cytoskeletal  
519 defects may promote cellular longevity and help reduce the senescent cell burden during  
520 organismal aging.

521         In contrast to the negative impacts of cellular senescence on aging, the anti-proliferative

522 effects of senescence can serve as a positive form of tumor suppression [96]. Several  
523 therapeutics that induce senescence in cancer cells have been developed to reduce and  
524 prevent metastatic growth [97]. The human *CDKN2A* locus, which encodes p16<sup>INK4A</sup>/Arf, is  
525 frequently inactivated or epigenetically suppressed in various types of cancers [98]. Thus, the  
526 *ArpC2* floxed *Cdkn2a* null cells used in our studies present a unique opportunity to study Arp2/3  
527 complex function in a genetic background that is particularly relevant to preventing the growth of  
528 cancer cells. Enhancing our understanding of the connection between the actin cytoskeleton  
529 and cellular senescence will therefore provide insight into therapeutic strategies used to  
530 regulate cell proliferation, arrest, and death in the context of both age-related diseases and  
531 cancers.

## 532 **Materials and Methods**

### 533 **Ethics statement**

534 Research with biological materials was approved by the UConn Institutional Biosafety  
535 Committee. This study did not include research with human subjects or live animals.

### 536 **Mammalian cell culture**

537 MTFs containing the floxed *ArpC2* allele (from James Bear, University of North Carolina) [42]  
538 were cultured in DMEM (with 4.5g/L glucose, L-Glutamine, 110mg/L sodium pyruvate), 10%  
539 fetal bovine serum (FBS), GlutaMAX, and antibiotic-antimycotic (Gibco). Cells were treated with  
540 media containing 0.01% DMSO or 2 $\mu$ M 4-OHT (Sigma) to obtain Flox or iKO populations. For  
541 treatments exceeding 3 days, culture supernatants were replaced with fresh media containing  
542 DMSO or 4-OHT on day 4. Cultures were returned to normal media after day 6. All experiments  
543 were performed using cells that had been in active culture for 2-12 trypsinized passages.

### 544 **Cell proliferation assays**

545 MTFs were cultured in 12-well plates and cell titers were routinely determined using a  
546 hemocytometer. Cells were initially seeded at multiple concentrations ranging from 2x10<sup>3</sup> to  
547 2x10<sup>4</sup> cells per well. After 5 days, confluent Flox samples were subcultured daily into multiple  
548 wells at concentrations of 1-2x10<sup>4</sup> cells per well, while iKO samples were subcultured if/when  
549 they reached 95% confluency. All cultures were expanded into 6-well plates and 6cm dishes  
550 when necessary. Population doubling times were calculated based on initial and final cell titers  
551 every 24-48h using the equation  $[\text{time} \times \log(2)] / [\log(\text{final}) - \log(\text{initial})]$ . Due to their continuous  
552 proliferation, the plotted values of cell numbers for Flox samples at days 8-12 were  
553 extrapolations based on doubling rates at those time points. For cGAS inhibitor experiments,  
554 MTF supernatants were replaced with fresh media containing 5 $\mu$ M RU.521 every 12h from days  
555 4-6 after 4-OHT exposure and counted at 0, 24, and 48h of DMSO or RU.521 treatment.

### 556 **Transfections and fluorescent probes**



557 For mCherry-cGAS cloning, mouse cGAS was amplified via PCR from a pMSCVpuro-eGFP-  
558 cGAS template (Addgene, 108675) using primers containing KpnI and NotI restriction sites (S1  
559 Table), and inserted into the pKC-mCherryC1 vector [99]. For transfections, Flox cells were  
560 grown in 12-well plates for 24h and then transfected with 350ng of mCherry-cGAS plasmid in  
561 DMEM. After 3h, DMEM was replaced with MTF media, and 18h later cells were trypsinized and  
562 transferred onto 12mm glass coverslips in 24-well plates. Media containing DMSO or 4-OHT  
563 was added after 3h, and cells were subjected to additional 29h growth before fixation as  
564 described below. For H2B-GFP transfections, Flox cells were grown in 24-well plates for 24h  
565 and then transfected with 130ng of H2B-GFP plasmid (Addgene, 11680). After 5h, DMEM was  
566 replaced with MTF media containing DMSO or 4-OHT. Cells were imaged live 15-40h later, as  
567 described below. All plasmids were maintained in NEB5-alpha *E.coli* and purified using  
568 Macherey-Nagel kits. For imaging acidic cytoplasmic organelles, cells were incubated for 30min  
569 in media containing 100nM LysoTracker Red (Invitrogen) prior to fixation.

#### 570 **RT-PCR and RT-qPCR**

571 RNA from Flox and iKO fibroblasts grown in 6-well plates was isolated using TRIzol reagent  
572 (Ambion). Following chloroform extraction, isopropanol precipitation, and a 75% ethanol wash,  
573 total RNA was resuspended in water. cDNA was reverse transcribed using the iScript cDNA  
574 synthesis kit (Bio-Rad) and then PCR-amplified using Taq polymerase (New England Biolabs)  
575 and primers listed in S1 Table. Primers were designed to amplify ~340-480bp with each cDNA  
576 target. The resulting PCR products were visualized on ethidium-bromide stained agarose gels.  
577 RT-qPCR was performed using SYBR-green (Bio-Rad) on a CFX96 Real-Time System (Bio-  
578 Rad). 1µl of cDNA was used in each 10µl RT-qPCR reaction, and all samples were run in  
579 duplicate. Primer dilution curves were analyzed to ensure primer specificity. Ct values were  
580 normalized to GAPDH and/or actin. The iKO:Flox ratio (fold difference) at each timepoint was  
581 calculated by the comparative  $\Delta\Delta$  cycle threshold method.

#### 582 **Cell extracts**

583 For preparation of whole cell extracts, fibroblasts cultured in 6-well plates were collected in  
584 phosphate buffered saline (PBS) containing 1mM EDTA, centrifuged at 2,900rpm for 5.5min at  
585 4°C, and lysed in 25mM HEPES (pH 7.4), 100mM NaCl, 1% Triton-X-100, 1mM EDTA, 1mM  
586 Na<sub>3</sub>VO<sub>4</sub>, 1mM NaF, 1mM phenylmethylsulfonyl fluoride, and 10µg/ml each of aprotinin,  
587 leupeptin, pepstatin, and chymostatin on ice. Lysates were mixed with Laemmli sample buffer,  
588 boiled, and centrifuged prior to SDS-PAGE analyses.

### 589 **Immunoblotting**

590 Cell extract samples were separated on 12% SDS-PAGE gels before transfer to nitrocellulose  
591 membranes (GE Healthcare). Membranes were blocked in PBS containing 5% milk before  
592 probing with primary antibodies at concentrations listed in [S2 Table](#). Following overnight  
593 incubation at 4°C, membranes were washed and treated with IRDye-680/800- (LI-COR) or  
594 horseradish peroxidase-conjugated (GE Healthcare) secondary antibodies. Infrared and  
595 chemiluminescent bands were visualized using a LI-COR Odyssey Fc Imaging System. Band  
596 intensities were measured using LI-COR Image Studio software. Densitometries of proteins-of-  
597 interest were normalized to GAPDH, tubulin, and/or actin loading controls.

### 598 **Immunostaining**

599 For immunofluorescence, fibroblasts cultured on glass coverslips in 24-well plates were washed  
600 with PBS and fixed using PBS containing 2.5% paraformaldehyde for 30min. Following PBS  
601 washes, cells were permeabilized using PBS containing 0.1% Triton X-100 for 2min, washed,  
602 and stained with primary antibodies in PBS containing 1% bovine serum albumin, 1% FBS, and  
603 0.02% azide for 45-60min as described in [S2 Table](#). Cells were washed and treated with Alexa  
604 Fluor 488-, 555-, or 647-conjugated goat anti-rabbit, anti-mouse, or anti-rat secondary  
605 antibodies, 1µg/mL DAPI, and/or 0.2U/mL Alexa Fluor 488- or 647-labeled phalloidin  
606 (Invitrogen) for 35-45min as detailed in [S2 Table](#). Following washes, coverslips were mounted  
607 on glass slides in Prolong Gold anti-fade (Invitrogen).

### 608 **Fluorescence microscopy**

609 All fixed and live cells were imaged using a Nikon Eclipse Ti microscope equipped with Plan  
610 Apo 100X (1.45 NA), Plan Apo 60X (1.40 NA), or Plan Fluor 20X (0.5 NA) objectives, an Andor  
611 Clara-E camera, and a computer running NIS Elements Software. Most images were taken as  
612 single epifluorescence slices, whereas 60X images of mCherry-transfected cells (Fig 7) were  
613 taken as z-stacks with a 0.3 $\mu$ m step size, and fixed mitotic cells were taken with a 0.3 $\mu$ m (Fig 9)  
614 or 0.5 $\mu$ m (Fig 8, Fig 10) step size. Live cell imaging was performed in a 35°C chamber (Okolab).  
615 During live imaging, cells were cultured in fresh media containing 25mM HEPES (pH 7.4) and  
616 DMSO or 4-OHT. Images were captured using the 20x objective at 12min intervals. All image  
617 processing and analysis was conducted using ImageJ/FIJI software [100].

### 618 **Fluorescence quantification**

619 Microscopic quantifications were performed using ImageJ. For fibroblast area calculations, cell  
620 perimeters were outlined based on phalloidin staining. For Lamin B1 abundance, the mean  
621 fluorescence intensity (MFI) of Lamin B1 staining in the nuclear area of the cell was measured  
622 and the background signal from outside the cell was subtracted from the MFI values. For  
623 normalization purposes, all MFI values for individual Flox and iKO cells were divided by the  
624 overall average MFI across 2 replicates for Flox cells. For acidic organelle analyses, the number  
625 of cells with diffuse LysoTracker staining was scored as positive or negative and divided by the  
626 total number of cells analyzed. To determine the LysoTracker area as a % of the total cell area,  
627 cell perimeters were outlined based on phalloidin staining and the Threshold tool was used to  
628 quantify the % of this area containing LysoTracker staining. For micronuclei and  $\gamma$ H2AX  
629 quantifications, the number of cells with DAPI-stained micronuclei and the number of cells with  
630 prominent nuclear  $\gamma$ H2AX clusters were quantified and divided by the total number of cells  
631 analyzed. Clusters were defined as isolated and discrete regions of  $\gamma$ H2AX staining. For  
632 analyses of p21, the MFI of p21 staining in the nuclear area of the cell was measured and the  
633 average p21 MFI across 3 replicates for Flox and iKO cells was calculated. The average MFI of

634 Flox cells was set to 1. For area-based assays of F-actin and microtubule intensities during  
635 metaphase, the DAPI-stained DNA mass was outlined in ImageJ and the MFI of phalloidin and  
636 anti-tubulin staining in this area was measured relative to DAPI. In linescan analyses of F-actin,  
637 tubulin, ArpC2, and DNA staining intensities in metaphase and/or anaphase cells, the ImageJ  
638 plot-profile tool was used. For metaphase, 14-16 $\mu$ m lines were drawn across the chromatin  
639 mass. For anaphase, 10-15 $\mu$ m lines were drawn across the mitotic spindle halfway between  
640 one set of chromosomes and the equator of the two forming daughter cells. In each plot, the  
641 minimum pixel intensity recorded along the line was subtracted from all values along the line to  
642 set the minimum to 0, and then all values were divided by the maximum to set the highest peak  
643 to 1. The numbers of cells analyzed in each type of assay are listed in the Figure Legends.

#### 644 **$\beta$ -galactosidase assays**

645 SA- $\beta$ gal activity was assessed using the Senescence  $\beta$ -Galactosidase Staining Kit (Cell  
646 Signaling Technologies, 9860). Fibroblasts were cultured in 6-well plates, washed once with  
647 PBS, fixed for 20min, and washed twice with PBS before incubation in SA- $\beta$ gal staining solution  
648 at 37°C in the dark for 20-24h. Images were captured using an iPhone 7 on a bright-field  
649 microscope equipped with a 10x objective. The % of SA- $\beta$ gal-positive cells was quantified by  
650 counting the number of intensely blue-colored cells divided by the total number of cells.  
651 Samples were coded and scored in a blinded fashion.

#### 652 **Reproducibility and Statistics**

653 All conclusions were based on observations made from at least 4 separate experiments, while  
654 quantifications were based on data from 2-5 representative experiments. Statistical analyses  
655 were performed using GraphPad Prism software as noted in the Figure Legends. P-values for  
656 data sets including 2 conditions were determined using unpaired t-tests unless otherwise noted.  
657 Analyses of data sets involving +/- scoring used Fisher's exact test. P-values <0.05 were  
658 considered statistically significant.

## 659 **Acknowledgements**

660 We thank Jim Bear (UNC Chapel Hill) for providing cells harboring the floxed *ArpC2* allele, Ming  
661 Xu (UConn Health) for comments on senescence experiments, Tom Maresca (UMass Amherst)  
662 for input on mitosis experiments, Tom Perrotta for support with writing, and Campellone Lab  
663 members for their suggestions related to this manuscript.

## 664 **References**

- 665 1. Pollard TD. Actin and Actin-Binding Proteins. Cold Spring Harb Perspect Biol. 2016 Aug  
666 1;8(8):a018226.
- 667 2. Campellone KG, Welch MD. A nucleator arms race: cellular control of actin assembly. Nat  
668 Rev Mol Cell Biol. 2010 Apr;11(4):237-51.
- 669 3. Welch MD, DePace AH, Verma S, Iwamatsu A, Mitchison TJ. The human Arp2/3 complex is  
670 composed of evolutionarily conserved subunits and is localized to cellular regions of dynamic  
671 actin filament assembly. J Cell Biol. 1997 Jul 28;138(2):375-84.
- 672 4. Abella JV, Galloni C, Pernier J, Barry DJ, Kjær S, Carlier MF, Way M. Isoform diversity in the  
673 Arp2/3 complex determines actin filament dynamics. Nat Cell Biol. 2016 Jan;18(1):76-86.
- 674 5. Schwob E, Martin RP. New yeast actin-like gene required late in the cell cycle. Nature. 1992  
675 Jan 9;355(6356):179-82.
- 676 6. Winter DC, Choe EY, Li R. Genetic dissection of the budding yeast Arp2/3 complex: a  
677 comparison of the in vivo and structural roles of individual subunits. Proc Natl Acad Sci U S A.  
678 1999 Jun 22;96(13):7288-93.
- 679 7. Zaki M, King J, Fütterer K, Insall RH. Replacement of the essential Dictyostelium Arp2 gene  
680 by its Entamoeba homologue using parasexual genetics. BMC Genet. 2007 Jun 6;8:28.
- 681 8. Hudson AM, Cooley L. A subset of dynamic actin rearrangements in Drosophila requires the  
682 Arp2/3 complex. J Cell Biol. 2002 Feb 18;156(4):677-87.
- 683 9. Stevenson V, Hudson A, Cooley L, Theurkauf WE. Arp2/3-dependent pseudocleavage  
684 [correction of psuedocleavage] furrow assembly in syncytial Drosophila embryos. Curr Biol.  
685 2002 Apr 30;12(9):705-11.
- 686 10. Sawa M, Suetsugu S, Sugimoto A, Miki H, Yamamoto M, Takenawa T. Essential role of the  
687 C. elegans Arp2/3 complex in cell migration during ventral enclosure. J Cell Sci. 2003 Apr  
688 15;116(Pt 8):1505-18.

- 689 11. Patel FB, Bernadskaya YY, Chen E, Jobanputra A, Pooladi Z, Freeman KL, Gally C, Mohler  
690 WA, Soto MC. The WAVE/SCAR complex promotes polarized cell movements and actin  
691 enrichment in epithelia during *C. elegans* embryogenesis. *Dev Biol.* 2008 Dec 15;324(2):297-  
692 309.
- 693 12. Yae K, Keng VW, Koike M, Yusa K, Kouno M, Uno Y, Kondoh G, Gotow T, Uchiyama Y,  
694 Horie K, Takeda J. Sleeping beauty transposon-based phenotypic analysis of mice: lack of  
695 *Arpc3* results in defective trophoblast outgrowth. *Mol Cell Biol.* 2006 Aug;26(16):6185-96.
- 696 13. Vauti F, Prochnow BR, Freese E, Ramasamy SK, Ruiz P, Arnold HH. Arp3 is required  
697 during preimplantation development of the mouse embryo. *FEBS Lett.* 2007 Dec  
698 11;581(29):5691-7.
- 699 14. Suraneni P, Rubinstein B, Unruh JR, Durnin M, Hanein D, Li R. The Arp2/3 complex is  
700 required for lamellipodia extension and directional fibroblast cell migration. *J Cell Biol.* 2012 Apr  
701 16;197(2):239-51.
- 702 15. Rotty JD, Wu C, Bear JE. New insights into the regulation and cellular functions of the  
703 ARP2/3 complex. *Nat Rev Mol Cell Biol.* 2013 Jan;14(1):7-12.
- 704 16. Kim IH, Racz B, Wang H, Burianek L, Weinberg R, Yasuda R, Wetsel WC, Soderling SH.  
705 Disruption of Arp2/3 results in asymmetric structural plasticity of dendritic spines and  
706 progressive synaptic and behavioral abnormalities. *J Neurosci.* 2013 Apr 3;33(14):6081-92.
- 707 17. Zhou K, Muroyama A, Underwood J, Leylek R, Ray S, Soderling SH, Lechler T. Actin-  
708 related protein2/3 complex regulates tight junctions and terminal differentiation to promote  
709 epidermal barrier formation. *Proc Natl Acad Sci U S A.* 2013 Oct 1;110(40):E3820-9.
- 710 18. Zhou K, Sumigray KD, Lechler T. The Arp2/3 complex has essential roles in vesicle  
711 trafficking and transcytosis in the mammalian small intestine. *Mol Biol Cell.* 2015 Jun  
712 1;26(11):1995-2004.
- 713 19. Wang PS, Chou FS, Ramachandran S, Xia S, Chen HY, Guo F, Suraneni P, Maher BJ, Li  
714 R. Crucial roles of the Arp2/3 complex during mammalian corticogenesis. *Development.* 2016

- 715 Aug 1;143(15):2741-52.
- 716 20. Papalazarou V, Swaminathan K, Jaber-Hijazi F, Spence H, Lahmann I, Nixon C, Salmeron-  
717 Sanchez M, Arnold HH, Rottner K, Machesky LM. The Arp2/3 complex is crucial for colonisation  
718 of the mouse skin by melanoblasts. *Development*. 2020 Nov 15;147(22):dev194555.
- 719 21. Mullins RD, Heuser JA, Pollard TD. The interaction of Arp2/3 complex with actin:  
720 nucleation, high affinity pointed end capping, and formation of branching networks of filaments.  
721 *Proc Natl Acad Sci U S A*. 1998 May 26;95(11):6181-6.
- 722 22. Machesky LM, Insall RH. Scar1 and the related Wiskott-Aldrich syndrome protein, WASP,  
723 regulate the actin cytoskeleton through the Arp2/3 complex. *Curr Biol*. 1998 Dec 17-  
724 31;8(25):1347-56.
- 725 23. Steffen A, Faix J, Resch GP, Linkner J, Wehland J, Small JV, Rottner K, Stradal TE.  
726 Filopodia formation in the absence of functional WAVE- and Arp2/3-complexes. *Mol Biol Cell*.  
727 2006 Jun;17(6):2581-91.
- 728 24. Nolen BJ, Tomasevic N, Russell A, Pierce DW, Jia Z, McCormick CD, Hartman J, Sakowicz  
729 R, Pollard TD. Characterization of two classes of small molecule inhibitors of Arp2/3 complex.  
730 *Nature*. 2009 Aug 20;460(7258):1031-4.
- 731 25. Hetrick B, Han MS, Helgeson LA, Nolen BJ. Small molecules CK-666 and CK-869 inhibit  
732 actin-related protein 2/3 complex by blocking an activating conformational change. *Chem Biol*.  
733 2013 May 23;20(5):701-12.
- 734 26. Belin BJ, Lee T, Mullins RD. DNA damage induces nuclear actin filament assembly by  
735 Formin -2 and Spire- $\frac{1}{2}$  that promotes efficient DNA repair. [corrected]. *Elife*. 2015 Aug  
736 19;4:e07735.
- 737 27. Caridi CP, D'Agostino C, Ryu T, Zapotoczny G, Delabaere L, Li X, Khodaverdian VY,  
738 Amaral N, Lin E, Rau AR, Chiolo I. Nuclear F-actin and myosins drive relocalization of  
739 heterochromatic breaks. *Nature*. 2018 Jul;559(7712):54-60.
- 740 28. Schrank BR, Aparicio T, Li Y, Chang W, Chait BT, Gundersen GG, Gottesman ME, Gautier



- 741 J. Nuclear ARP2/3 drives DNA break clustering for homology-directed repair. *Nature*. 2018  
742 Jul;559(7712):61-66.
- 743 29. King VL, Leclair NK, Coulter AM, Campellone KG. The actin nucleation factors JMY and  
744 WHAMM enable a rapid Arp2/3 complex-mediated intrinsic pathway of apoptosis. *PLoS Genet*.  
745 2021 Apr 19;17(4):e1009512.
- 746 30. Lénárt P, Bacher CP, Daigle N, Hand AR, Eils R, Terasaki M, Ellenberg J. A contractile  
747 nuclear actin network drives chromosome congression in oocytes. *Nature*. 2005 Aug  
748 11;436(7052):812-8.
- 749 31. Burdyniuk M, Callegari A, Mori M, Nédélec F, Lénárt P. F-Actin nucleated on chromosomes  
750 coordinates their capture by microtubules in oocyte meiosis. *J Cell Biol*. 2018 Aug  
751 6;217(8):2661-2674.
- 752 32. Azoury J, Lee KW, Georget V, Rassinier P, Leader B, Verlhac MH. Spindle positioning in  
753 mouse oocytes relies on a dynamic meshwork of actin filaments. *Curr Biol*. 2008 Oct  
754 14;18(19):1514-9.
- 755 33. Mogessie B, Schuh M. Actin protects mammalian eggs against chromosome segregation  
756 errors. *Science*. 2017 Aug 25;357(6353):eaal1647.
- 757 34. Kim HC, Jo YJ, Kim NH, Namgoong S. Small molecule inhibitor of formin homology 2  
758 domains (SMIFH2) reveals the roles of the formin family of proteins in spindle assembly and  
759 asymmetric division in mouse oocytes. *PLoS One*. 2015 Apr 2;10(4):e0123438.
- 760 35. Kita AM, Swider ZT, Erofeev I, Halloran MC, Goryachev AB, Bement WM. Spindle-F-actin  
761 interactions in mitotic spindles in an intact vertebrate epithelium. *Mol Biol Cell*. 2019 Jul  
762 1;30(14):1645-1654.
- 763 36. Farina F, Gaillard J, Guérin C, Couté Y, Sillibourne J, Blanchoin L, Théry M. The  
764 centrosome is an actin-organizing centre. *Nat Cell Biol*. 2016 Jan;18(1):65-75.
- 765 37. Plessner M, Knerr J, Grosse R. Centrosomal Actin Assembly Is Required for Proper Mitotic  
766 Spindle Formation and Chromosome Congression. *iScience*. 2019 May 31;15:274-281.

- 767 38. Farina F, Ramkumar N, Brown L, Samandar Eweis D, Anstatt J, Waring T, Bithell J, Scita  
768 G, Thery M, Blanchoin L, Zech T, Baum B. Local actin nucleation tunes centrosomal  
769 microtubule nucleation during passage through mitosis. *EMBO J.* 2019 Jun 3;38(11):e99843.
- 770 39. Inoue D, Obino D, Pineau J, Farina F, Gaillard J, Guerin C, Blanchoin L, Lennon-Duménil  
771 AM, Théry M. Actin filaments regulate microtubule growth at the centrosome. *EMBO J.* 2019  
772 Jun 3;38(11):e99630.
- 773 40. Wu C, Asokan SB, Berginski ME, Haynes EM, Sharpless NE, Griffith JD, Gomez SM, Bear  
774 JE. Arp2/3 is critical for lamellipodia and response to extracellular matrix cues but is  
775 dispensable for chemotaxis. *Cell.* 2012 Mar 2;148(5):973-87.
- 776 41. Wu C, Haynes EM, Asokan SB, Simon JM, Sharpless NE, Baldwin AS, Davis IJ, Johnson  
777 GL, Bear JE. Loss of Arp2/3 induces an NF- $\kappa$ B-dependent, nonautonomous effect on  
778 chemotactic signaling. *J Cell Biol.* 2013 Dec 23;203(6):907-16.
- 779 42. Rotty JD, Wu C, Haynes EM, Suarez C, Winkelman JD, Johnson HE, Haugh JM, Kovar  
780 DR, Bear JE. Profilin-1 serves as a gatekeeper for actin assembly by Arp2/3-dependent and -  
781 independent pathways. *Dev Cell.* 2015 Jan 12;32(1):54-67.
- 782 43. Dimchev V, Lahmann I, Koestler SA, Kage F, Dimchev G, Steffen A, Stradal TEB, Vauti F,  
783 Arnold HH, Rottner K. Induced Arp2/3 Complex Depletion Increases FMNL2/3 Formin  
784 Expression and Filopodia Formation. *Front Cell Dev Biol.* 2021 Feb 1;9:634708.
- 785 44. Gournier H, Goley ED, Niederstrasser H, Trinh T, Welch MD. Reconstitution of human  
786 Arp2/3 complex reveals critical roles of individual subunits in complex structure and activity. *Mol*  
787 *Cell.* 2001 Nov;8(5):1041-52.
- 788 45. Hayflick L, Moorhead PS. The serial cultivation of human diploid cell strains. *Exp Cell Res.*  
789 1961 Dec;25:585-621.
- 790 46. Hayflick L. The limited in vitro lifetime of human diploid cell strains. *Exp Cell Res.* 1965  
791 Mar;37:614-36.
- 792 47. Coppé JP, Patil CK, Rodier F, Sun Y, Muñoz DP, Goldstein J, Nelson PS, Desprez PY,

- 793 Campisi J. Senescence-associated secretory phenotypes reveal cell-nonautonomous functions  
794 of oncogenic RAS and the p53 tumor suppressor. *PLoS Biol.* 2008 Dec 2;6(12):2853-68.
- 795 48. Kuilman T, Michaloglou C, Vredeveld LC, Douma S, van Doorn R, Desmet CJ, Aarden LA,  
796 Mooi WJ, Peeper DS. Oncogene-induced senescence relayed by an interleukin-dependent  
797 inflammatory network. *Cell.* 2008 Jun 13;133(6):1019-31.
- 798 49. Coppé JP, Desprez PY, Krtolica A, Campisi J. The senescence-associated secretory  
799 phenotype: the dark side of tumor suppression. *Annu Rev Pathol.* 2010;5:99-118.
- 800 50. Basisty N, Kale A, Jeon OH, Kuehnemann C, Payne T, Rao C, Holtz A, Shah S, Sharma V,  
801 Ferrucci L, Campisi J, Schilling B. A proteomic atlas of senescence-associated secretomes for  
802 aging biomarker development. *PLoS Biol.* 2020 Jan 16;18(1):e3000599.
- 803 51. Freund A, Laberge RM, Demaria M, Campisi J. Lamin B1 loss is a senescence-associated  
804 biomarker. *Mol Biol Cell.* 2012;23(11):2066-2075.
- 805 52. Dimri GP, Lee X, Basile G, Acosta M, Scott G, Roskelley C, Medrano EE, Linskens M,  
806 Rubelj I, Pereira-Smith O, et al. A biomarker that identifies senescent human cells in culture and  
807 in aging skin in vivo. *Proc Natl Acad Sci U S A.* 1995 Sep 26;92(20):9363-7.
- 808 53. Lee BY, Han JA, Im JS, Morrone A, Johung K, Goodwin EC, Kleijer WJ, DiMaio D, Hwang  
809 ES. Senescence-associated beta-galactosidase is lysosomal beta-galactosidase. *Aging Cell.*  
810 2006 Apr;5(2):187-95.
- 811 54. Kurz DJ, Decary S, Hong Y, Erusalimsky JD. Senescence-associated (beta)-galactosidase  
812 reflects an increase in lysosomal mass during replicative ageing of human endothelial cells. *J*  
813 *Cell Sci.* 2000 Oct;113 ( Pt 20):3613-22.
- 814 55. Hernandez-Segura A, Nehme J, Demaria M. Hallmarks of Cellular Senescence. *Trends*  
815 *Cell Biol.* 2018 Jun;28(6):436-453.
- 816 56. DiMicco R, Krizhanovsky V, Baker D, d'Adda di Fagagna F. Cellular senescence in ageing:  
817 from mechanisms to therapeutic opportunities. *Nat Rev Mol Cell Biol.* 2021 Feb;22(2):75-95.
- 818 57. Kumari R, Jat P. Mechanisms of Cellular Senescence: Cell Cycle Arrest and Senescence

- 819 Associated Secretory Phenotype. *Front Cell Dev Biol.* 2021 Mar 29;9:645593.
- 820 58. Ivanov A, Pawlikowski J, Manoharan I, van Tuyn J, Nelson DM, Rai TS, Shah PP, Hewitt G,  
821 Korolchuk VI, Passos JF, Wu H, Berger SL, Adams PD. Lysosome-mediated processing of  
822 chromatin in senescence. *J Cell Biol.* 2013 Jul 8;202(1):129-43.
- 823 59. Dou Z, Ghosh K, Vizioli MG, et al. Cytoplasmic chromatin triggers inflammation in  
824 senescence and cancer. *Nature.* 2017 Oct 19;550(7676):402-406.
- 825 60. Miller KN, Dasgupta N, Liu T, Adams PD, Vizioli MG. Cytoplasmic chromatin fragments-  
826 from mechanisms to therapeutic potential. *Elife.* 2021 Jan 29;10:e63728.
- 827 61. Rogakou EP, Pilch DR, Orr AH, Ivanova VS, Bonner WM. DNA double-stranded breaks  
828 induce histone H2AX phosphorylation on serine 139. *J Biol Chem.* 1998 Mar 6;273(10):5858-68.
- 829 62. Kasthuber ER, Lowe SW. Putting p53 in Context. *Cell.* 2017 Sep;170(6):1062-78.
- 830 63. Hafner A, Bulyk ML, Jambhekar A, Lahav G. The multiple mechanisms that regulate p53  
831 activity and cell fate. *Nat Rev Mol Cell Biol.* 2019 Apr;20(4):199-210.
- 832 64. Beauséjour CM, Krtolica A, Galimi F, Narita M, Lowe SW, Yaswen P, Campisi J. Reversal  
833 of human cellular senescence: roles of the p53 and p16 pathways. *EMBO J.* 2003 Aug  
834 15;22(16):4212-22.
- 835 65. Wang, B., Wang, L., Gasek, N.S. *et al.* An inducible *p21*-Cre mouse model to monitor and  
836 manipulate *p21*-highly-expressing senescent cells in vivo. *Nat Aging* **1**, 962–973 (2021).
- 837 66. Abbas T, Dutta A. p21 in cancer: intricate networks and multiple activities. *Nat Rev Cancer.*  
838 2009 Jun;9(6):400–14.
- 839 67. El-Deiry WS. p21(WAF1) Mediates Cell-Cycle Inhibition, Relevant to Cancer Suppression  
840 and Therapy. *Cancer Res.* 2016 Sep 15;76(18):5189-91.
- 841 68. Chen Q, Sun L, Chen ZJ. Regulation and function of the cGAS-STING pathway of cytosolic  
842 DNA sensing. *Nat Immunol.* 2016 Sep 20;17(10):1142-9.
- 843 69. Hopfner KP, Hornung V. Molecular mechanisms and cellular functions of cGAS-STING  
844 signalling. *Nat Rev Mol Cell Biol.* 2020 Sep;21(9):501-521.

- 845 70. Glück S, Guey B, Gulen MF, Wolter K, Kang TW, Schmacke NA, Bridgeman A, Rehwinkel  
846 J, Zender L, Ablasser A. Innate immune sensing of cytosolic chromatin fragments through cGAS  
847 promotes senescence. *Nat Cell Biol.* 2017 Sep;19(9):1061-1070.
- 848 71. Mackenzie KJ, Carroll P, Martin CA, Murina O, Fluteau A, Simpson DJ, Olova N, Sutcliffe  
849 H, Rainger JK, Leitch A, Osborn RT, Wheeler AP, Nowotny M, Gilbert N, Chandra T, Reijns  
850 MAM, Jackson AP. cGAS surveillance of micronuclei links genome instability to innate  
851 immunity. *Nature.* 2017 Aug 24;548(7668):461-465.
- 852 72. Li T, Chen ZJ. The cGAS-cGAMP-STING pathway connects DNA damage to inflammation,  
853 senescence, and cancer. *J Exp Med.* 2018;215(5):1287-1299.
- 854 73. Volkman HE, Cambier S, Gray EE, Stetson DB. Tight nuclear tethering of cGAS is essential  
855 for preventing autoreactivity. *Elife.* 2019 Dec 6;8:e47491.
- 856 74. de Oliveira Mann CC, Hopfner KP. Nuclear cGAS: guard or prisoner? *EMBO J.* 2021 Aug  
857 16;40(16):e108293.
- 858 75. Taguchi T, Mukai K, Takaya E, Shindo R. STING Operation at the ER/Golgi Interface. *Front*  
859 *Immunol.* 2021 May 3;12:646304.
- 860 76. Vincent J, Adura C, Gao P, Luz A, Lama L, Asano Y, Okamoto R, Imaeda T, Aida J,  
861 Rothamel K, Gogakos T, Steinberg J, Reasoner S, Aso K, Tuschl T, Patel DJ, Glickman JF,  
862 Ascano M. Small molecule inhibition of cGAS reduces interferon expression in primary  
863 macrophages from autoimmune mice. *Nat Commun.* 2017 Sep 29;8(1):750.
- 864 77. Fenech M, Kirsch-Volders M, Natarajan AT, Surralles J, Crott JW, Parry J, Norppa H,  
865 Eastmond DA, Tucker JD, Thomas P. Molecular mechanisms of micronucleus, nucleoplasmic  
866 bridge and nuclear bud formation in mammalian and human cells. *Mutagenesis.* 2011  
867 Jan;26(1):125-32.
- 868 78. Utani K, Okamoto A, Shimizu N. Generation of micronuclei during interphase by coupling  
869 between cytoplasmic membrane blebbing and nuclear budding. *PLoS One.* 2011  
870 Nov;6(11):e27233.

- 871 79. Crasta K, Ganem NJ, Dagher R, et al. DNA breaks and chromosome pulverization from  
872 errors in mitosis. *Nature*. 2012 Feb 2;482(7383):53-58.
- 873 80. Liu S, Pellman D. The coordination of nuclear envelope assembly and chromosome  
874 segregation in metazoans. *Nucleus*. 2020 Dec;11(1):35-52.
- 875 81. Gorgoulis V, Adams PD, Alimonti A, Bennett DC, Bischof O, Bishop C, Campisi J, Collado  
876 M, Evangelou K, Ferbeyre G, Gil J, Hara E, Krizhanovsky V, Jurk D, Maier AB, Narita M,  
877 Niedernhofer L, Passos JF, Robbins PD, Schmitt CA, Sedivy J, Vougas K, von Zglinicki T, Zhou  
878 D, Serrano M, Demaria M. Cellular Senescence: Defining a Path Forward. *Cell*. 2019  
879 Oct;179(4):813-827.
- 880 82. Swaney KF, Li R. Function and regulation of the Arp2/3 complex during cell migration in  
881 diverse environments. *Curr Opin Cell Biol*. 2016;42:63-72.
- 882 83. Moore AS, Holzbaur ELF. Mitochondrial-cytoskeletal interactions: dynamic associations that  
883 facilitate network function and remodeling. *Curr Opin Physiol*. 2018 Jun;3:94-100.
- 884 84. Chakrabarti R, Lee M, Higgs HN. Multiple roles for actin in secretory and endocytic  
885 pathways. *Curr Biol*. 2021 May 24;31(10):R603-R618.
- 886 85. Basile JR, Eichten A, Zacny V, Munger K. NF-kappaB-mediated induction of  
887 p21(Cip1/Waf1) by tumor necrosis factor alpha induces growth arrest and cytoprotection in  
888 normal human keratinocytes. *Mol Cancer Res*. 2003 Feb;1(4):262-70.
- 889 86. Jackson JG, Pereira-Smith OM. p53 is preferentially recruited to the promoters of growth  
890 arrest genes p21 and GADD45 during replicative senescence of normal human fibroblasts.  
891 *Cancer Res*. 2006 Sep 1;66(17):8356-60.
- 892 87. Rovillain E, Mansfield L, Caetano C, Alvarez-Fernandez M, Caballero OL, Medema RH,  
893 Hummerich H, Jat PS. Activation of nuclear factor-kappa B signalling promotes cellular  
894 senescence. *Oncogene*. 2011 May 19;30(20):2356-66.
- 895 88. Basit A, Cho MG, Kim EY, Kwon D, Kang SJ, Lee JH. The cGAS/STING/TBK1/IRF3 innate  
896 immunity pathway maintains chromosomal stability through regulation of p21 levels. *Exp Mol*

- 897 Med. 2020 Apr;52(4):643-657.
- 898 89. Rieder CL, Maiato H. Stuck in division or passing through: what happens when cells cannot  
899 satisfy the spindle assembly checkpoint. *Dev Cell*. 2004 Nov;7(5):637-51.
- 900 90. Collado M, Blasco MA, Serrano M. Cellular senescence in cancer and aging. *Cell*. 2007 Jul  
901 27;130(2):223-33.
- 902 91. Baker DJ, Wijshake T, Tchkonia T, LeBrasseur NK, Childs BG, van de Sluis B, Kirkland JL,  
903 van Deursen JM. Clearance of p16Ink4a-positive senescent cells delays ageing-associated  
904 disorders. *Nature*. 2011 Nov 2;479(7372):232-6.
- 905 92. Baker DJ, Childs BG, Durik M, Wijers ME, Sieben CJ, Zhong J, Saltness RA, Jeganathan  
906 KB, Verzosa GC, Pezeshki A, Khazaie K, Miller JD, van Deursen JM. Naturally occurring  
907 p16(Ink4a)-positive cells shorten healthy lifespan. *Nature*. 2016 Feb 11;530(7589):184-9.
- 908 93. Hickson LJ, Langhi Prata LGP, Bobart SA, Evans TK, Giorgadze N, Hashmi SK, Herrmann  
909 SM, Jensen MD, Jia Q, Jordan KL, Kellogg TA, Khosla S, Koerber DM, Lagnado AB, Lawson  
910 DK, LeBrasseur NK, Lerman LO, McDonald KM, McKenzie TJ, Passos JF, Pignolo RJ,  
911 Pirtskhalava T, Saadiq IM, Schaefer KK, Textor SC, Vitorcelli SG, Volkman TL, Xue A,  
912 Wentworth MA, Wissler Gerdes EO, Zhu Y, Tchkonia T, Kirkland JL. Senolytics decrease  
913 senescent cells in humans: Preliminary report from a clinical trial of Dasatinib plus Quercetin in  
914 individuals with diabetic kidney disease. *EBioMedicine*. 2019 Sep;47:446-456.
- 915 94. Baird NA, Douglas PM, Simic MS, Grant AR, Moresco JJ, Wolff SC, Yates JR 3rd, Manning  
916 G, Dillin A. HSF-1-mediated cytoskeletal integrity determines thermotolerance and life span.  
917 *Science*. 2014 Oct 17;346(6207):360-3.
- 918 95. Higuchi-Sanabria R, Paul JW 3rd, Durieux J, Benitez C, Frankino PA, Tronnes SU, Garcia  
919 G, Daniele JR, Monshietehadi S, Dillin A. Spatial regulation of the actin cytoskeleton by HSF-1  
920 during aging. *Mol Biol Cell*. 2018 Oct 15;29(21):2522-2527.
- 921 96. Hinds P, Pietruska J. Senescence and tumor suppression. *F1000Res*. 2017 Dec 11;6:2121.
- 922 97. Saleh T, Bloukh S, Carpenter VJ, Alwohoush E, Bakeer J, Darwish S, Azab B, Gewirtz DA.

- 923 Therapy-Induced Senescence: An "Old" Friend Becomes the Enemy. *Cancers* (Basel). 2020  
924 Mar 29;12(4):822.
- 925 98. Ko A, Han SY, Song J. Dynamics of ARF regulation that control senescence and  
926 cancer. *BMB Rep.* 2016 Nov;49(11):598-606.
- 927 99. Campellone KG, Webb NJ, Znameroski EA, Welch MD. WHAMM is an Arp2/3 complex  
928 activator that binds microtubules and functions in ER to Golgi transport. *Cell.* 2008  
929 Jul;134(1):148-161.
- 930 100. Schindelin J, Arganda-Carreras I, Frise E, Kaynig V, Longair M, Pietzsch T, Preibisch S,  
931 Rueden C, Saalfeld S, Schmid B, Tinevez JY, White DJ, Hartenstein V, Eliceiri K, Tomancak P,  
932 Cardona A. Fiji: an open-source platform for biological-image analysis. *Nat Methods.* 2012 Jun  
933 28;9(7):676-82.



## 934 **Figure Legends**

935 **Fig 1. ArpC2 iKO cells undergo a proliferation arrest and enlargement. (A)** Mouse  
936 fibroblasts were treated with DMSO (Flox) or 4-OHT (iKO) for 0-6d and collected at 0-13d.  
937 Samples were lysed, subjected to SDS-PAGE, and immunoblotted with antibodies to ArpC2,  
938 Arp3, and GAPDH. **(B)** ArpC2 and Arp3 band intensities were normalized to GAPDH or tubulin  
939 band intensities and plotted as the iKO:Flox ratio. Each dot represents the mean ratio  $\pm$ SD from  
940 2-3 experiments. **(C)** Flox and iKO cells were fixed at 7d and stained with phalloidin (F-actin;  
941 magenta), an Arp3 antibody (green), and DAPI (DNA; blue). The arrowhead highlights a  
942 micronucleus. Scale bar, 10 $\mu$ m. **(D)** Flox and iKO cell titers were quantified at 0-18d. Each point  
943 represents the mean  $\pm$ SD from 2 Flox and 2-3 iKO experiments, except for the 14d and 18d  
944 timepoints, which were from a representative iKO sample that did not exhibit outgrowth of  
945 colonies expressing ArpC2. **(E)** Flox and iKO population doubling times were quantified daily  
946 from 0-4d and 5-12d. For each time range, the bar represents the mean doubling time  $\pm$ SD from  
947 n=3 experiments. **(F)** Flox and iKO cells were fixed at 7d and stained with phalloidin and DAPI.  
948 The arrowhead highlights a micronucleus. Scale bar, 25 $\mu$ m. **(G)** Flox and iKO cells were  
949 outlined in ImageJ and their areas quantified. Each dot represents an individual cell and the  
950 lines represent the mean area  $\pm$ SD from analyses of 100 cells.

951

952 **Fig 2. Loss of the Arp2/3 complex results in elevated *Il-6* transcript and decreased**  
953 **nuclear Lamin B1 levels. (A)** Mouse fibroblasts were treated with DMSO (Flox) or 4-OHT  
954 (iKO) for 0-6d and collected at 0, 3, 6, and 9d. RNA was isolated and RT-PCR performed using  
955 primers for *Il-6* and *Gapdh*. PCR products were visualized on ethidium bromide stained agarose  
956 gels. **(B)** RT-qPCR was performed using primers for *Il-6* and *Gapdh* at 9d. *Il-6* product levels  
957 were normalized to *Gapdh*. Each bar represents the mean transcript abundance  $\pm$ SD from n=3  
958 experiments. AU = Arbitrary Units. **(C)** Flox and iKO cells were collected at 10d and

959 immunoblotted with antibodies to Lamin B1, ArpC2, GAPDH, and actin. **(D)** Lamin B1 band  
960 intensity was normalized to GAPDH and actin band intensities. Each bar represents the mean  
961 intensity  $\pm$ SD from n=3 experiments. **(E)** Flox and iKO cells were fixed at 9d and stained with a  
962 Lamin B1 antibody (green) and DAPI (DNA; blue). Arrowheads point to micronuclei. Scale bar,  
963 25 $\mu$ m. **(F)** Nuclear Lamin B1 levels were quantified by outlining the DAPI-stained nucleus of  
964 each cell in ImageJ and measuring the mean Lamin B1 pixel intensity. Each dot represents an  
965 individual cell and the line depicts the average Lamin B1 pixel intensity from analyses of 492-  
966 556 cells pooled from n=2 experiments (denoted in black or green). RFU = Relative  
967 Fluorescence Units.

968

969 **Fig 3. SA- $\beta$ gal activity and lysosomal content are increased in ArpC2 iKO cells. (A)**  
970 Mouse fibroblasts were treated with DMSO (Flox) or 4-OHT (iKO) for 0-6d and senescence-  
971 associated beta-galactosidase (SA- $\beta$ gal) staining was performed over a 22d period. **(B)** The %  
972 of SA- $\beta$ gal-positive cells was quantified by calculating the number of intensely blue-colored cells  
973 divided by the total number of cells. Each point represents the mean %  $\pm$ SD from a  
974 representative 0d timepoint, n=2 experiments for the 3d and 22d timepoints, and  
975 n=3 experiments for the 7d and 13d timepoints (727-2197 cells per point). **(C)** Flox and iKO  
976 cells at 9d were treated with LysoTracker (magenta), fixed, and stained with DAPI (DNA; blue).  
977 The magnifications illustrate punctate versus diffuse LysoTracker staining, and the arrowhead  
978 indicates the position of a micronucleus. Scale bars, 25 $\mu$ m. **(D)** The % of cells exhibiting diffuse  
979 LysoTracker staining was quantified by scoring the number of cells with broad instead of  
980 punctate cytoplasmic fluorescence and dividing by the total number of cells. The relative area  
981 within each cell occupied by LysoTracker was quantified using the threshold function in ImageJ.  
982 Each bar represents the mean %  $\pm$ SD from n=2 experiments (151-155 cells per bar).

983 **Fig 4. Arp2/3 complex depletion leads to the formation of cytoplasmic micronuclei. (A)**  
984 Mouse fibroblasts were treated with DMSO (Flox) or 4-OHT (iKO) for 6d, fixed at 7d, and  
985 stained with DAPI. Arrowheads point to micronuclei. Scale bar, 25 $\mu$ m. **(B)** Magnifications show  
986 different micronucleus phenotypes in iKO cells. Scale bar, 5 $\mu$ m. **(C)** The % of cells with  
987 micronuclei was quantified over a 13d period following DMSO or 4-OHT exposure. Each point  
988 represents the mean %  $\pm$ SD from n=3 experiments, except for the 2d and 4d timepoints, which  
989 are from n=2 experiments (432-631 cells per point in each experiment).  
990

991 **Fig 5. Prominent DNA damage clusters are found in the nuclei and micronuclei of ArpC2**  
992 **iKO cells. (A)** Mouse fibroblasts were treated with DMSO (Flox) or 4-OHT (iKO) for 6d, fixed at  
993 7d, and stained with a  $\gamma$ H2AX antibody (green) and DAPI (DNA; blue). Arrowheads point to  
994  $\gamma$ H2AX clusters in micronuclei and arrows indicate  $\gamma$ H2AX clusters in nuclei. Scale bar, 25 $\mu$ m.  
995 **(B)** Magnifications show no or diffuse  $\gamma$ H2AX staining in Flox nuclei and  $\gamma$ H2AX clusters in iKO  
996 cell nuclei and micronuclei. Scale bar, 5 $\mu$ m. **(C)** The % of cells with  $\gamma$ H2AX clusters was  
997 quantified over a 13d period following DMSO or 4-OHT exposure. Each point represents the  
998 mean %  $\pm$ SD from n=3 experiments, except for 2d and 4d timepoints, which are from n=2  
999 experiments (432-631 cells per point in each experiment).  
1000

1001 **Fig 6. Activation of p53 and upregulation of *Cdkn1a/p21* occur in ArpC2 iKO cells. (A)**  
1002 Mouse fibroblasts were treated with DMSO (Flox) or 4-OHT (iKO) for 3d, collected, and  
1003 immunoblotted with antibodies to p53, phospho-p53(Ser15), ArpC2, tubulin, actin, and GAPDH.  
1004 Total and phosphorylated p53 intensities relative to loading controls are indicated beneath the  
1005 respective bands. **(B)** Flox and iKO cells were fixed at 3d and stained with a p53 antibody  
1006 (green) and DAPI (DNA; blue). Arrowheads point to micronuclei. Scale bars, 25 $\mu$ m. **(C)** Flox  
1007 and iKO cells were collected at 0, 3, 6, and 9d. RNA was isolated and RT-PCR performed using

1008 primers for *Cdkn1a*, *Gapdh* and  $\beta$ -*actin*. PCR products were visualized on ethidium bromide  
1009 stained agarose gels. **(D)** RT-qPCR was performed using primers for *Cdkn1a* and *Gapdh* at 0,  
1010 3, 6, and 9d. *Cdkn1a* product levels were normalized to *Gapdh* and plotted as the iKO:Flox  
1011 ratio. Each point represents the mean ratio  $\pm$ SD from n=3 experiments. **(E)** Flox and iKO cells  
1012 were fixed at 6d and stained with a p21 antibody (green) and DAPI. **(F)** Nuclear p21  
1013 fluorescence was quantified by outlining the DAPI-stained nucleus of each cell in ImageJ and  
1014 measuring the mean p21 pixel intensity. Each bar represents the mean intensity  $\pm$ SD from n=3  
1015 experiments (653-658 cells per bar). RFU = Relative Fluorescence Units.

1016  
1017 **Fig 7. cGAS and STING are recruited to micronuclei.** **(A)** Mouse fibroblasts were treated  
1018 with 4-OHT (iKO), transfected with plasmids encoding mCherry or mCherry-cGAS, collected,  
1019 and immunoblotted with antibodies to mCherry and GAPDH. **(B)** iKO cells expressing mCherry  
1020 or mCherry-cGAS (magenta) were fixed at 1-2d and stained with DAPI (DNA; blue). Arrowheads  
1021 point to a cGAS-positive micronucleus. Scale bars, 20 $\mu$ m. **(C)** Cells were treated with DMSO  
1022 (Flox) or 4-OHT (iKO) for 3-4d and immunoblotted with antibodies to cGAS, STING, ArpC2,  
1023 tubulin, actin, and GAPDH. **(D)** Flox and iKO cells were fixed at 3d and stained with cGAS  
1024 (magenta) or STING (green) antibodies and DAPI. Arrowheads point to cGAS- or STING-  
1025 positive micronuclei. 38.7% of micronuclei-containing iKO cells were cGAS-positive (75 cells  
1026 from n=2 experiments). Insets show STING localization around an iKO micronucleus. **(E)** iKO  
1027 cells were fixed at 3d and stained with STING antibodies (green) and either a GRP94 or GM130  
1028 antibody (yellow). **(F)** Cells were treated with DMSO or 4-OHT for 3d, switched to media  
1029 containing DMSO or RU.521, and population doubling times were quantified daily from 4-6d.  
1030 Each bar represents the mean doubling time  $\pm$ SD from n=5 experiments.

1031

1032 **Fig 8. Micronuclei form due to chromatin segregation errors and premature mitotic exits**  
1033 **in ArpC2 iKO cells. (A-B)** Live H2B-GFP-expressing mouse fibroblasts were imaged every  
1034 12min from 1-2d following DMSO (Flox) or 4-OHT (iKO) exposure. Panel A shows completed  
1035 mitoses, while panel B shows iKO cells exiting mitosis prematurely. Arrowheads in the final 3-6  
1036 frames point to micronuclei biogenesis events. Scale bars, 5 $\mu$ m. **(C)** The % of completed  
1037 mitoses yielding micronuclei was calculated by dividing the number of mitoses yielding at least  
1038 one micronucleus by the total number of completed mitoses captured during live imaging (Flox  
1039 n=63; iKO n=52; pooled from 13 Flox and 22 iKO experiments). **(D)** All completed mitoses of  
1040 Flox and iKO cells were binned into categories based on the number of timepoints observed in  
1041 metaphase (Flox n=63; iKO n=52). Black and grey bars represent Flox and iKO data,  
1042 respectively. **(E)** The % of premature mitotic exits was calculated by dividing the number of  
1043 cells that entered prophase and returned to interphase without completing anaphase by the total  
1044 number of cells that entered prophase (Flox n=71; iKO n=70; pooled from 13 Flox and 22 iKO  
1045 experiments). 10 of the 70 iKO cells (14.3%) formed micronuclei. **(F)** iKO cells were fixed at 7d  
1046 and stained with a  $\gamma$ H2AX antibody (green) and DAPI (DNA; blue). Movies for panels A and B  
1047 appear in Supporting Information (S1-S7 Videos).

1048

1049 **Fig 9. Arp2/3 complex depletion reduces actin filament density in the chromatin-**  
1050 **containing central spindle during metaphase. (A)** Mouse fibroblasts were treated with  
1051 DMSO for 1-2d, fixed, and stained with phalloidin (F-actin; magenta), an anti-tubulin antibody  
1052 (microtubules; green), anti-ArpC2 antibodies (yellow), and DAPI (DNA; blue). Images represent  
1053 the lower, middle, and upper regions of metaphase cells. Scale bars, 5 $\mu$ m. **(B)** The DNA-  
1054 containing region was isolated from the middle spindle in A, magnified, and subjected to line-  
1055 scan fluorescence intensity analyses. Plot profiles depict the pixel intensity values for tubulin  
1056 (green), F-actin (magenta), ArpC2 (yellow), and DNA (blue) along the dashed lines drawn  
1057 across the representative metaphase region. Color-coded arrowheads highlight the overlapping

1058 peaks of tubulin, F-actin, and ArpC2 and the inverse intensity pattern for DNA. RFU = Relative  
1059 Fluorescence Units. **(C)** Mouse fibroblasts were treated with DMSO (Flox) or 4-OHT (iKO) for  
1060 1-2d, fixed, and stained with phalloidin, an anti-tubulin antibody, and DAPI. The chromatin mass  
1061 at the central metaphase spindle was outlined in ImageJ (dashed shapes) or a plot-profile line  
1062 was drawn through it (dashed line). The bottom DAPI-stained iKO cell panel was overexposed  
1063 in order to draw attention to the presence of 2 chromatin fragments erroneously missing from  
1064 the metaphase plate (arrowheads). **(D)** Fluorescence intensities of F-actin and microtubules  
1065 were measured in chromatin areas outlined as in panel C. Each bar represents the mean  
1066 intensity  $\pm$ SD from n=12 metaphase chromatin regions compiled from 3 experiments. **(E)** Plot  
1067 profiles performed as in panel B depict the pixel intensity values for tubulin, F-actin, and DNA  
1068 along the dashed lines drawn across the metaphase region from the representative iKO cell in  
1069 panel C.

1070

1071 **Fig 10. Anaphase microtubules are unbalanced in ArpC2 iKO cells.** **(A)** Mouse fibroblasts  
1072 were treated with DMSO (Flox) or 4-OHT (iKO) for 1d, fixed, and stained with a tubulin antibody  
1073 (green) and DAPI (DNA; blue). Scale bar, 5 $\mu$ m. **(B)** Line-scan plot profiles depict the pixel  
1074 intensity of tubulin along the horizontal dashed lines drawn across the representative mitotic  
1075 spindles from panel A. Arrowheads highlight sites of aberrant chromatin localization. RFU =  
1076 Relative Fluorescence Units.

1077 **Supporting Information Captions**

1078

1079 **S1 Table. Primers.**

1080

1081 **S2 Table. Immunofluorescence and immunoblotting reagents.**

1082

1083 **S1 Video. Timelapse movie of a H2B-GFP-expressing Flox cell (see Fig 8A first row).**

1084

1085 **S2 Video. Timelapse movie of a H2B-GFP-expressing Flox cell (see Fig 8A second row).**

1086

1087 **S3 Video. Timelapse movie of a H2B-GFP-expressing iKO cell (see Fig 8A third row).**

1088

1089 **S4 Video. Timelapse movie of a H2B-GFP-expressing iKO cell (see Fig 8A fourth row).**

1090

1091 **S5 Video. Timelapse movie of a H2B-GFP-expressing iKO cell (see Fig 8B first row).**

1092

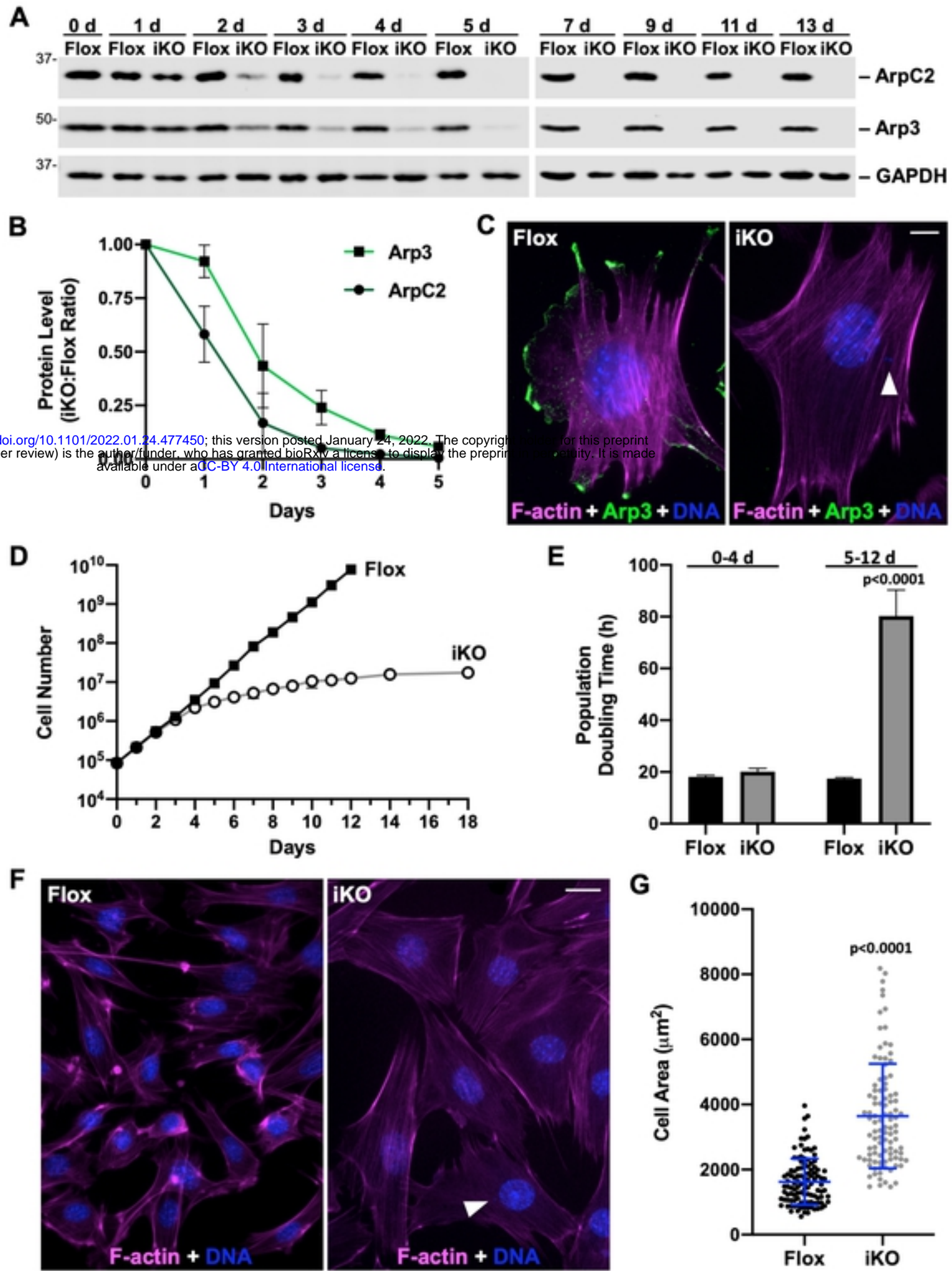
1093 **S6 Video. Timelapse movie of a H2B-GFP-expressing iKO cell (see Fig 8B second row).**

1094

1095 **S7 Video. Timelapse movie of a H2B-GFP-expressing iKO cell (see Fig 8B third row).**

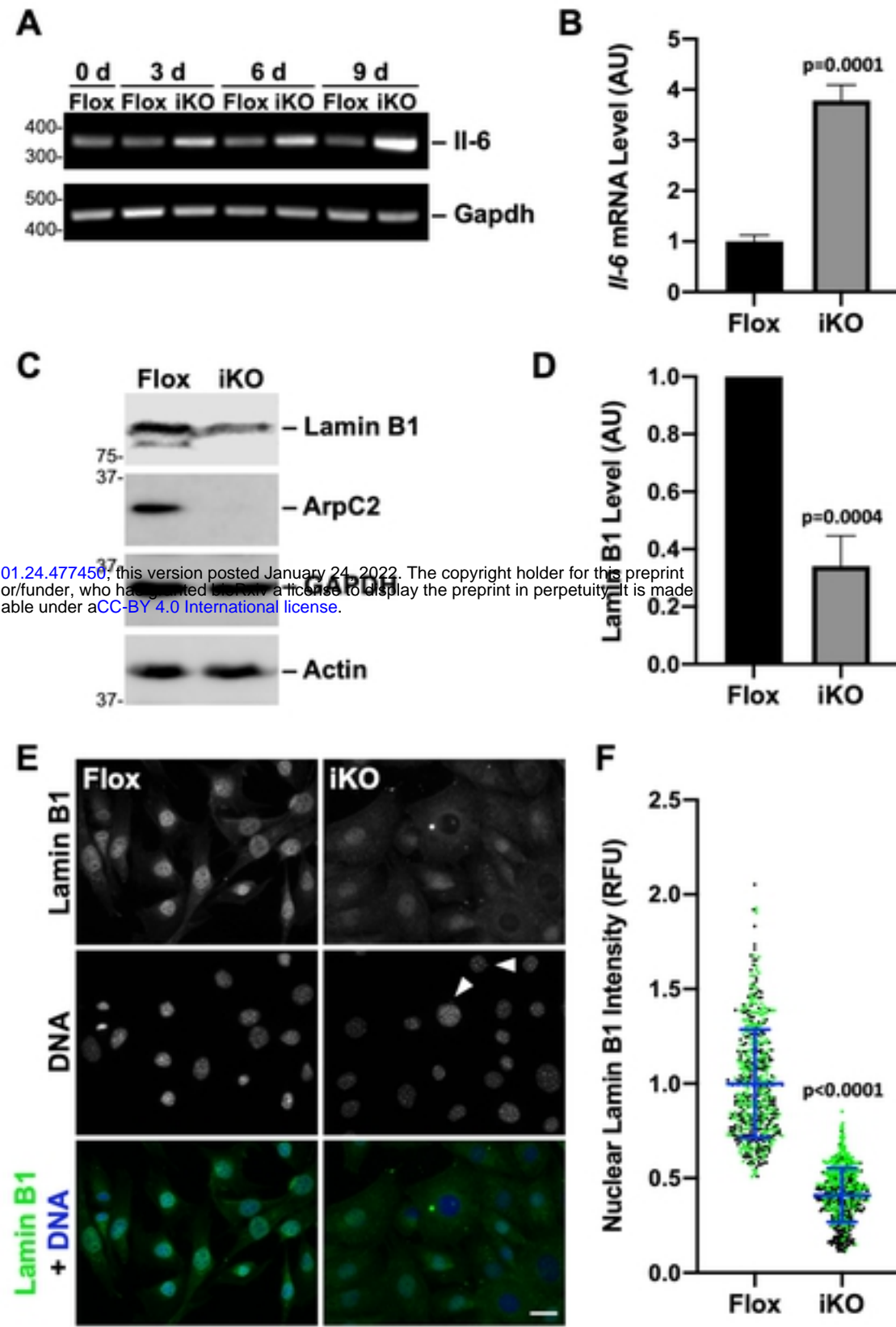


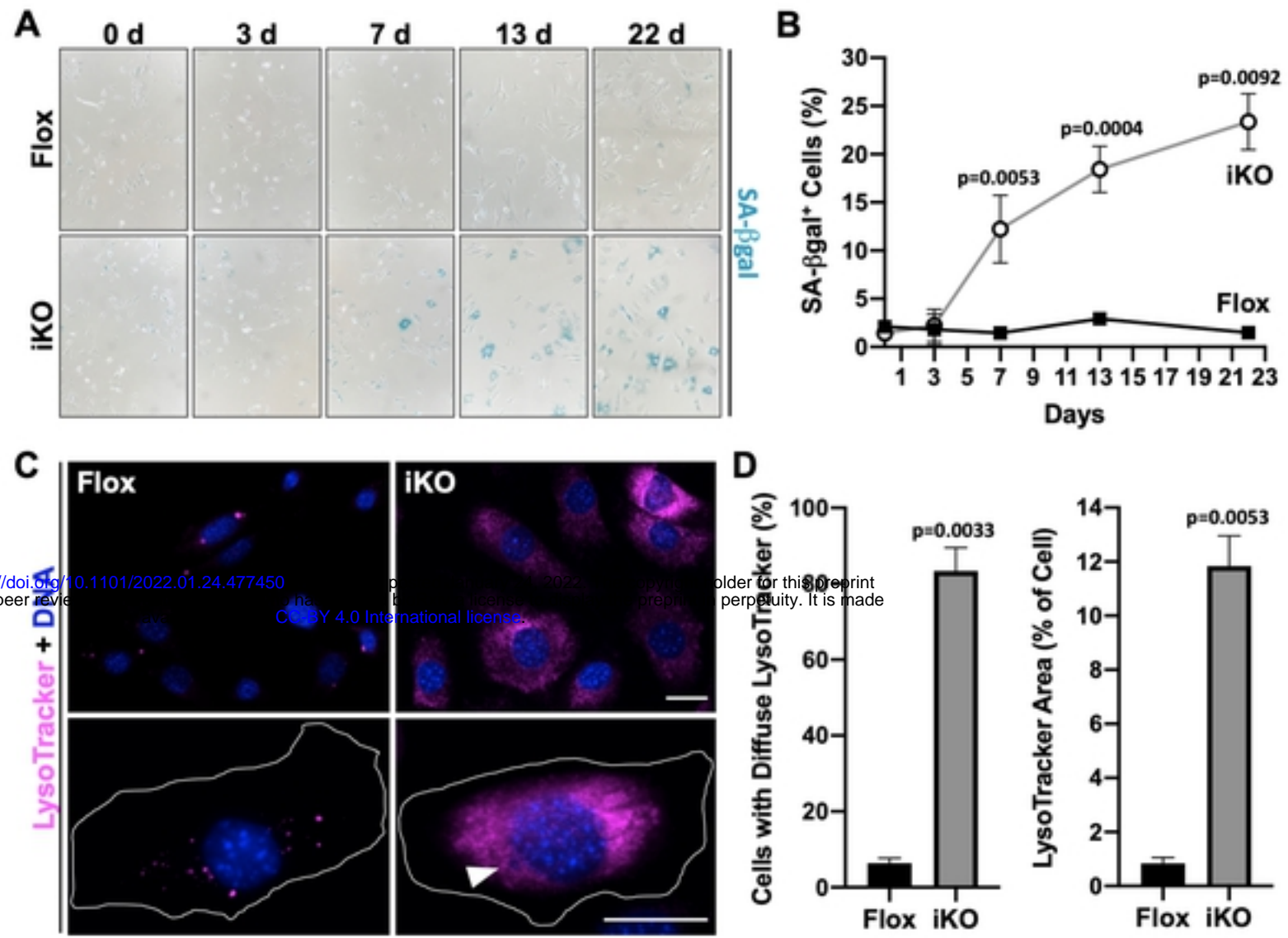
bioRxiv preprint doi: <https://doi.org/10.1101/2022.01.24.477450>; this version posted January 24, 2022. The copyright holder for this preprint (which was not certified by peer review) is the author/funder, who has granted bioRxiv a license to display the preprint in perpetuity. It is made available under aCC-BY 4.0 International license.

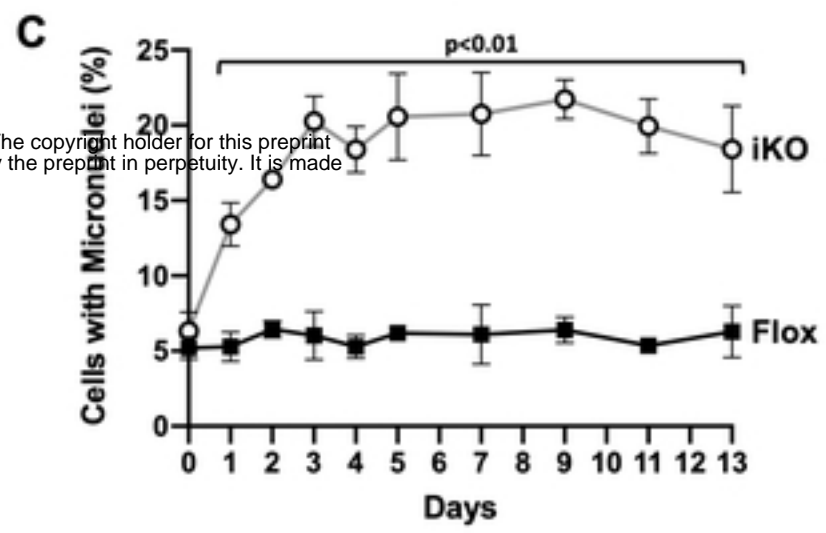
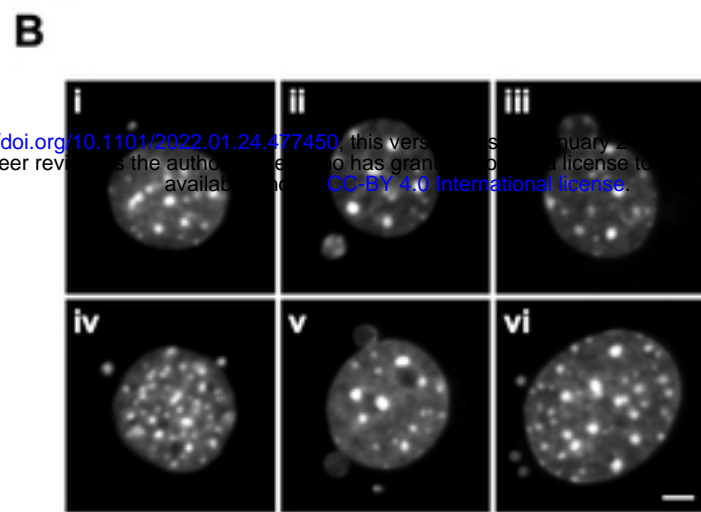
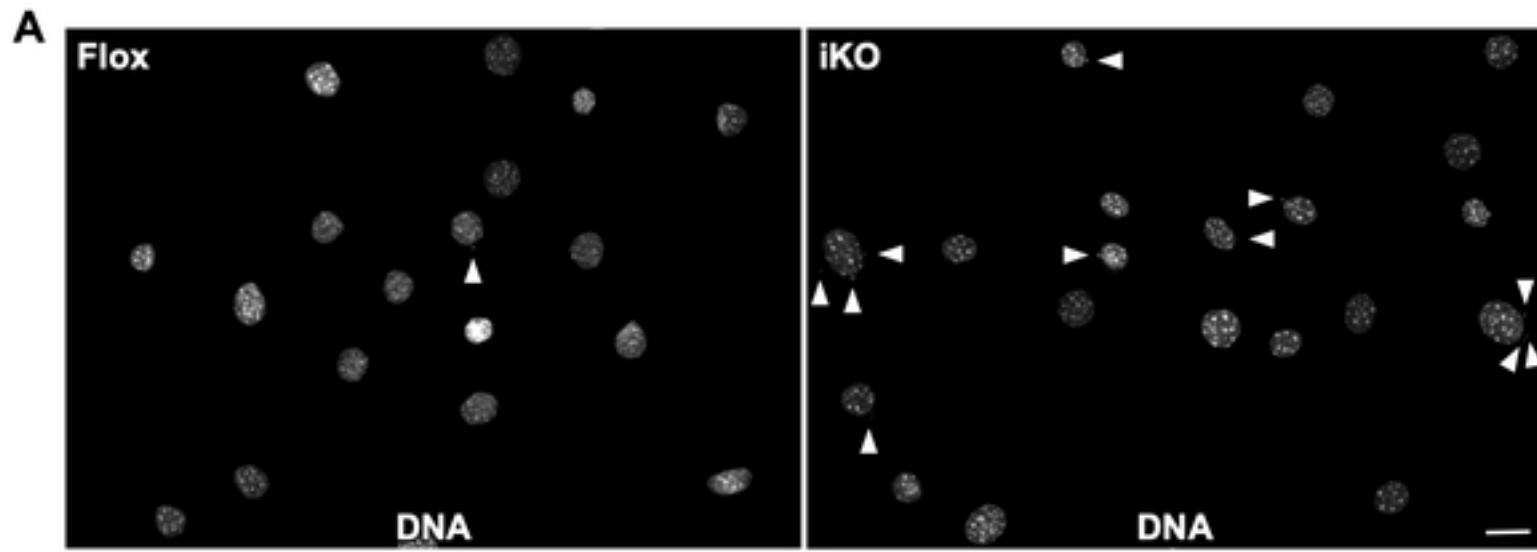




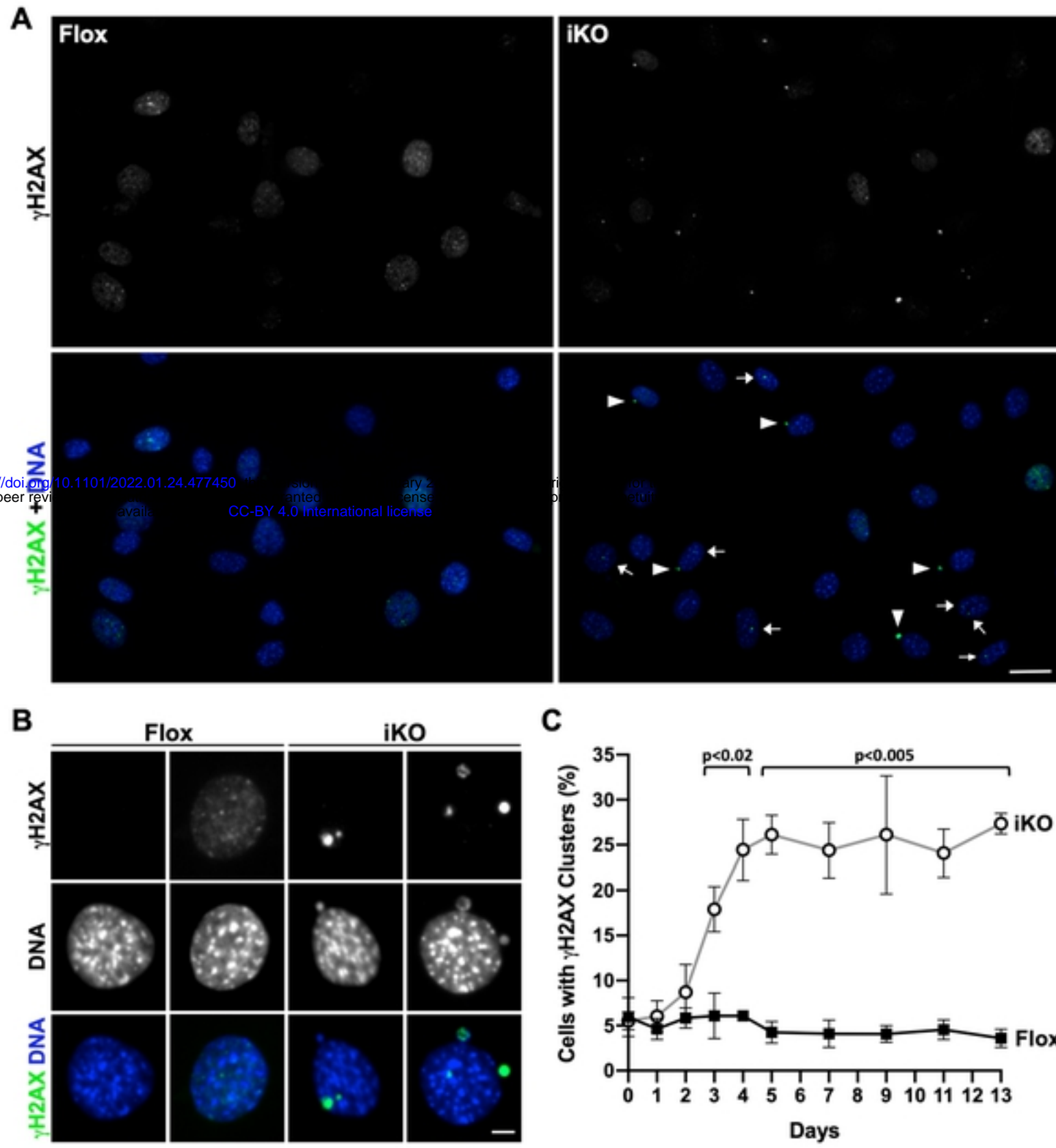
bioRxiv preprint doi: <https://doi.org/10.1101/2022.01.24.477450>; this version posted January 24, 2022. The copyright holder for this preprint (which was not certified by peer review) is the author/funder, who has granted bioRxiv a license to display the preprint in perpetuity. It is made available under aCC-BY 4.0 International license.

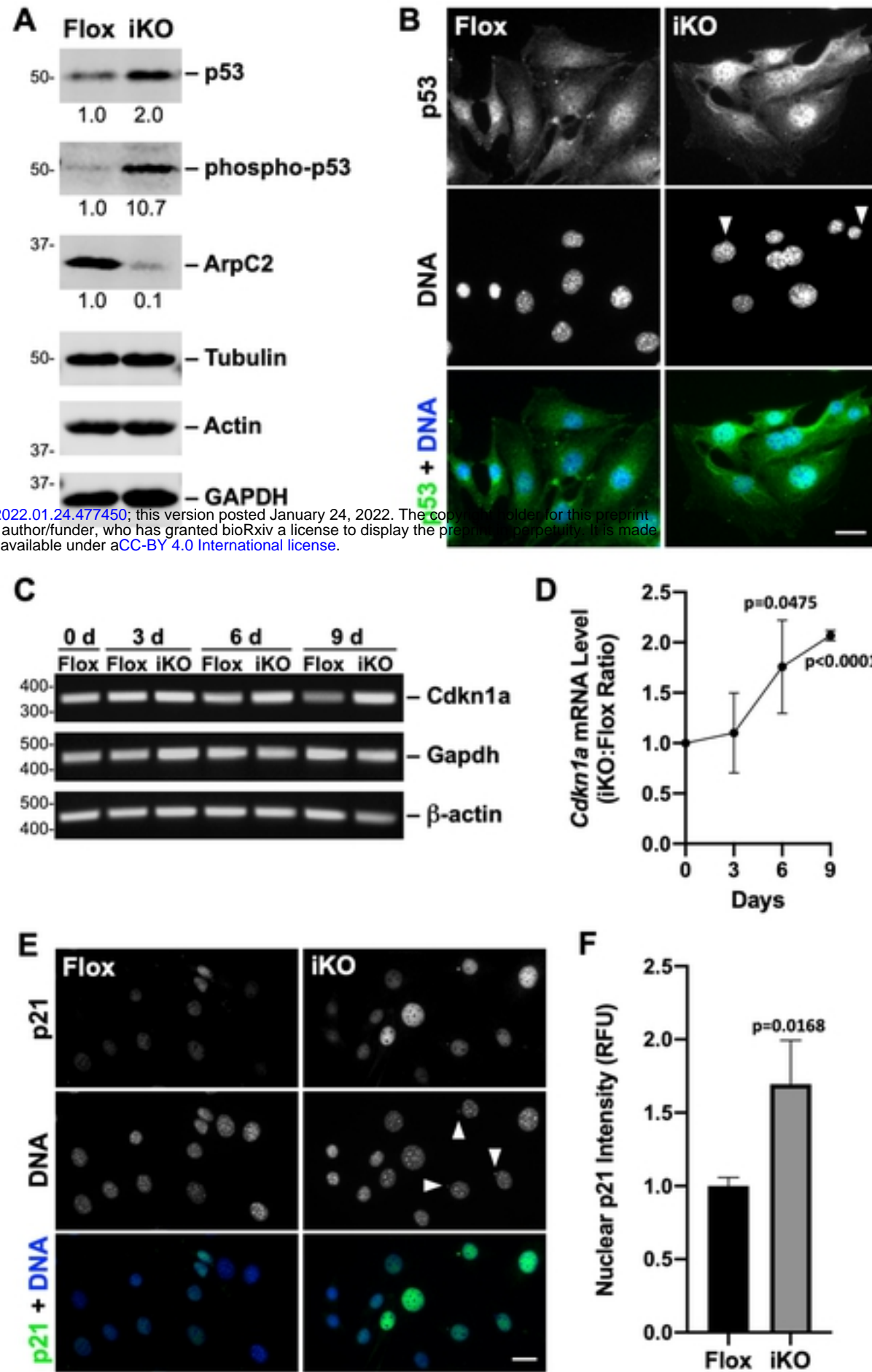




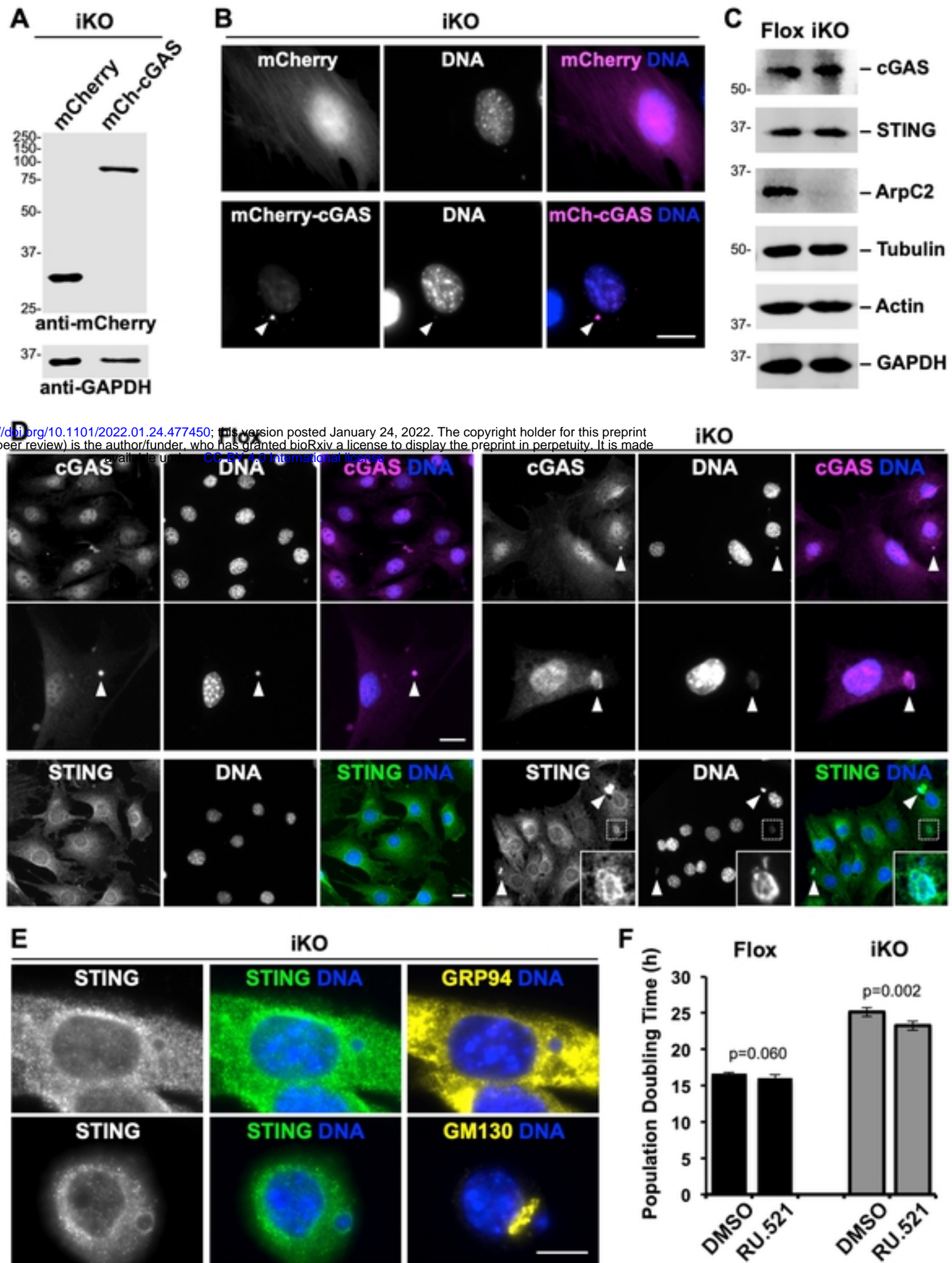


bioRxiv preprint doi: <https://doi.org/10.1101/2022.01.24.477450>; this version posted January 24, 2022. The copyright holder for this preprint (which was not certified by peer review) is the author/funder, who has granted bioRxiv a license to display the preprint in perpetuity. It is made available under aCC-BY 4.0 International license.









bioRxiv preprint doi: <https://doi.org/10.1101/2022.01.24.477450>; this version posted January 24, 2022. The copyright holder for this preprint (which was not certified by peer review) is the author/funder, who has granted bioRxiv a license to display the preprint in perpetuity. It is made available under aCC-BY 4.0 International license.

